J. Fluid Mech. (2007), *vol.* 592, *pp.* 295–334. © 2007 Cambridge University Press
doi:10.1017/S0022112007008476 Printed in the United Kingdom

Heated falling films

P. M. J. TREVELYAN[1]†, B. SCHEID[2]‡, C. RUYER-QUIL[3] AND S. KALLIADASIS[1]

[1]Department of Chemical Engineering, Imperial College London, London, SW7 2AZ, UK

[2]Service de Chimie-Physique E.P., Université Libre de Bruxelles, C.P. 165/62, 1050 Brussels, Belgium

[3]Laboratoire FAST, UMR 7608, CNRS, Universités P. et M. Curie et Paris Sud, Bât. 502, Campus Universitaire, 91405 Orsay Cedex, France

ptrevely@ulb.ac.be; bscheid@ulb.ac.be, ruyer@fast.u-psud.fr; s.kalliadasis@imperial.ac.uk

(Received 5 October 2006 and in revised form 1 August 2007)

We present new insights and results for the problem of a film falling down a heated wall: (i) treatment of a mixed heat flux boundary condition on the substrate; (ii) development of a long-wave theory for large Péclet numbers; (iii) refined treatment of the energy equation based on a high-order Galerkin projection in terms of polynomial test functions which satisfy all boundary conditions; (iv) time-dependent computations for the free-surface height and interfacial temperature; (v) numerical solution of the full energy equation; (vi) demonstration of the existence of a thermal boundary layer at the front stagnation point of a solitary pulse; (vii) development of models that prevent negative temperatures and are in good agreement with the numerical solution of the full energy equation.

1. Introduction

1.1. *Isothermal films*

The dynamics of an isothermal film falling down a planar substrate is driven by the classical long-wave instability mode first observed in the pioneering experiments by Kapitza & Kapitza (1949). Benney (1966) was the first to apply to this problem an expansion with respect to the long-wave parameter ϵ. This expansion, frequently referred to as 'long-wave expansion' (LWE), leads to a single equation of the evolution type for the free surface. Later, Pumir, Manneville & Pomeau (1983) and Nakaya (1989) constructed numerically solitary waves of the first-order LWE and demonstrated that the solitary-wave solution branches for the speed of the waves as a function of the Reynolds number show branch multiplicity and turning points above which solitary waves do not exist. Further, time-dependent computations by Pumir *et al.* (1983) showed that LWE exhibits finite-time blow-up behaviour when this equation is integrated in regions of the parameter space where solitary waves do not exist. The connection between the absence of solitary-wave solutions and finite-time blow up was investigated by Scheid *et al.* (2004). Clearly, this behaviour is unrealistic and marks the failure of LWE to correctly describe nonlinear waves far from criticality – close

† Present address: Centre for Nonlinear Phenomena and Complex Systems, CP 231, Université Libre de Bruxelles, 1050 Brussels, Belgium.

‡ Present address: Division of Engineering and Applied Sciences, Harvard University, Cambridge, MA 02138, USA.

https://doi.org/10.1017/S0022112007008476 Published online by Cambridge University Press

to criticality, LWE is exact as far as critical/neutral conditions are concerned; this is not surprising as LWE is a regular perturbation expansion of the full Navier–Stokes equations. A review of the developments in isothermal falling films is given by Chang & Demekhin (2002).

Following the pioneering theoretical work by Kapitza (1948), an *ad hoc* but convenient simplification was employed by Shkadov (1967, 1968) who developed the integral-boundary-layer (IBL) approximation which combines the boundary-layer approximation of the Navier–Stokes equations assuming a self-similar parabolic velocity profile and long waves on the interface with the Kármán–Pohlhausen averaging method in boundary-layer theory. This procedure results in a two-equation model for the free surface and flow rate and unlike LWE, IBL has no turning points and predicts the existence of solitary waves for all Reynolds numbers. However, despite its success in describing nonlinear waves far from criticality, Shkadov's IBL approach does have some shortcomings with the principal one being an erroneous prediction of the critical Reynolds number. By combining a gradient expansion with a weighted residual technique using polynomial test functions, Ruyer-Quil & Manneville (2000, 2002) obtained a two-equation model having the same structural form as Shkadov's, but recovering correctly the instability threshold.

1.2. *Heated films*

The dynamics of a film falling down a heated wall is driven by both the Kapitza mode and the long-wave Marangoni mode obtained by Smith in his study of horizontal layers heated uniformly from below (Smith 1966). The nonlinear stage of the instability for the uniformly heated falling film was investigated by Joo, Davis & Bankoff (1991) who used the LWE to obtain an evolution equation for the film thickness. In addition to the Marangoni effect, these authors also included evaporation effects and long-range attractive intermolecular interactions. A review of a wide variety of fluid-flow problems using LWE, including problems with Marangoni effects, is given by Oron, Davis & Bankoff (1997).

The first study to investigate the dynamics of a film falling down a uniformly heated wall far from criticality was that of Kalliadasis *et al.* (2003*b*). Their analysis was based on the model equations derived by Kalliadasis *et al.* (2003*a*) for a falling film heated from below by a local heat source. These authors formulated an IBL approximation of the equations of motion by adopting a linear test function for the temperature field to obtain a weighted residuals approach for the energy equation yielding a three-equation model for the free surface, flow rate and interfacial temperature. However, despite this IBL model behaving well in the nonlinear regime, it does not predict neutral and critical conditions accurately and hence it suffers from the same limitations as the Shkadov model for the isothermal film. The limitations of the model equations derived by Kalliadasis *et al.* (2003*a*, *b*) were overcome by Ruyer-Quil *et al.* (2005) and Scheid *et al.* (2005). These authors also took into account the second-order dissipative effects in the momentum and energy equations. These second-order terms were neglected in the formulation by Kalliadasis *et al.* (2003*a*, *b*), but they play an important role in the dispersion of waves for larger Reynolds numbers. The procedure followed is effectively an extension of the methodology applied in the case of isothermal flows by Ruyer-Quil & Manneville (2000, 2002) and is based on a high-order weighted residuals approach with polynomial expansions for both velocity and temperature fields. Details of the theoretical developments are also given in Scheid (2004) which contains an extensive study of the heated-falling-film problem including the case of non-uniform heating (see also Kabov 1998; Scheid *et al.* 2002).

https://doi.org/10.1017/S0022112007008476 Published online by Cambridge University Press

1.3. *Outline*

Here we revisit the heated-falling-film problem. We impose two types of wall boundary conditions: a heat flux (HF) and a specified temperature (ST) condition. Note that all previous studies on the heated-falling-film problem imposed the ST condition only. Scheid (2004) first introduced HF. This condition involves the heat flux from the wall to the substrate and the heat losses from the wall to the ambient gas phase. Hence, it is a more realistic condition than the ST one. The two cases are contrasted and we demonstrate that they are similar only when heat transport convective effects can be neglected and for certain values of the Marangoni and Biot numbers. Further, we employ the same first order in ϵ single-mode Galerkin representation for the transport of momentum given by equations (5.17*a*) and (5.17*b*) in Scheid (2004) (and equations (4.18*a*) and (4.18*b*) in Ruyer-Quil *et al.* 2005). However, for the transport of heat, we develop a refined treatment of the energy equation for both HF and ST problems. This results in an alternative system of first order in ϵ amplitude equations obtained by introducing a new set of test functions which satisfy all boundary conditions so that our Galerkin approach incorporates the boundary conditions within its projection. On the other hand, the models derived in Scheid (2004) and Ruyer-Quil *et al.* (2005) adopted test functions which do not satisfy all boundary conditions. The Galerkin projection then incorporated the boundary conditions in the boundary terms resulting through integrations by parts following the averaging of the energy equation. Moreover, unlike the studies by Scheid (2004) and Ruyer-Quil *et al.* (2005) where the amplitudes in the expansion for the temperature field are assigned certain orders with respect to ϵ, in the projection for the temperature field presented here, the order of the amplitudes is not specified.

We demonstrate that the linear stability properties of a three-equation model (for the free surface, flow rate and interfacial temperature) obtained by a single-mode Galerkin projection is in good agreement with an Orr–Sommerfeld analysis of the linearized Navier–Stokes and energy equations. We also develop an LWE approximation which is used to ensure that the models obtained from our refined weighted residuals approach based on a high-order Galerkin projection yield LWE with an appropriate gradient expansion, thus confirming the validity of the models close to criticality. The LWE expansion is also used to contrast the HF and ST problems. Note that unlike all previous LWE theories in the area of heated thin films, e.g. Joo *et al.* (1991), which typically assume the Péclet number to be $O(1)$, our LWE equation is obtained by assuming a large Péclet number. Indeed, the Péclet number can be much larger than the Reynolds number owing to the ratio of the momentum to the thermal diffusivity being usually much larger than unity.

We construct bifurcation diagrams for travelling solitary waves and we demonstrate that LWE exhibits turning points and branch multiplicity or points where the solution branches terminate (this last feature has not been observed before in isothermal falling-film problems where the solution branches always exhibit turning points). On the other hand, the new three-equation model based on the single-mode Galerkin projection predicts the continuing existence of solitary waves for all Reynolds numbers. Further, the HF case shows the existence of negative-hump solitary waves in certain regions of the parameter space, unlike ST which only yields positive-hump waves (here we are referring to single-hump waves only). The predictions of the bifurcation diagrams are confirmed by time-dependent computations of the single-mode Galerkin projection model for both HF and ST (the previous studies by Kalliadasis *et al.* (2003*b*) and Scheid *et al.* (2005) on heated falling films focused on the construction of stationary solitary waves only, without any time-dependent computations). For the HF case,

https://doi.org/10.1017/S0022112007008476 Published online by Cambridge University Press

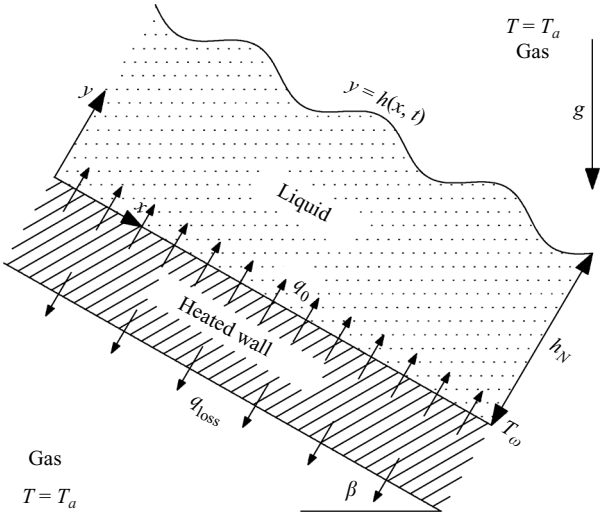


FIGURE 1. Sketch of the profile geometry for a thin liquid film falling down an inclined heated wall forming an angle β with the horizontal direction. h_N is the Nusselt flat film thickness. The surrounding gas phase is maintained at temperature T_a. For ST the heater maintains the wall temperature at T_w. For HF two heat fluxes contribute to the liquid temperature gradient at $y = 0$: the heat flux generated by the heater embedded in the wall, q_0, and the heat losses from the wall to the ambient gas, q_{loss}.

the system can evolve into negative-hump waves never observed in isothermal films (although such permanent solitary waves do exist, they are unstable in time-dependent computations (Chang & Demekhin 2002)).

Finally, we construct numerically the solution of the full energy equation at first order in ϵ which is after all the equation we are trying to model. This allows us to assess both the new single-mode Galerkin projection model developed here and the first-order temperature models given by equation (8.8) for HF and equation (5.17*c*) for ST from Scheid (2004) (see also equation (4.18*c*) for ST in Ruyer-Quil *et al.* 2005) (previous studies on the problem focused more on model development than validation in the nonlinear regime). The new model provides a substantially improved representation of the temperature field (and hence the flow field due to the coupling through the Marangoni effect) over the previous ones as the Reynolds number increases. The good agreement between our model and the numerical solution of the full energy equation at first order in ϵ persists up to a certain Reynolds number at which a recirculation zone appears in the crest of a solitary wave. As the recirculation zone grows, the model diverges from the actual solution and eventually predicts negative interfacial temperatures at some Reynolds number. This deficiency is cured with the introduction of modified weight functions prior to averaging. The resulting modified averaged models prevent the interfacial temperature from becoming negative and are in good agreement with the numerical solution of the full energy equation.

2. Problem definition

2.1. *Governing equations*

Figure 1 shows the flow situation. A heat source, e.g. an electric heating device, inside the plate uniformly generates heat. The surrounding gas phase below the plate and above the liquid film is maintained at a constant temperature T_a. The liquid has

https://doi.org/10.1017/S0022112007008476 Published online by Cambridge University Press

constant viscosity μ, density ρ, constant pressure heat capacity c_p, thermal diffusivity κ and thermal conductivity $\lambda = \rho c_p \kappa$, all assumed to be constant. We also assume that the liquid is non-volatile so that evaporation effects can be neglected, and the film is sufficiently thin that buoyancy effects can be neglected. A coordinate system (x, y) is chosen so that x is the streamwise coordinate and y is the outward-pointing coordinate normal to the wall. The wall is then located at $y = 0$ and the interface at $y = h(x, t)$. The governing equations are conservation of mass, Navier–Stokes and energy equations,

$$\nabla \cdot \boldsymbol{u} = 0, \quad \boldsymbol{u}_t + (\boldsymbol{u} \cdot \nabla)\boldsymbol{u} = -\frac{1}{\rho}\nabla p + \nu \nabla^2 \boldsymbol{u} + \boldsymbol{g} \tag{2.1a, b}$$

$$T_t + (\boldsymbol{u} \cdot \nabla)T = \kappa \nabla^2 T, \tag{2.1c}$$

where $\boldsymbol{u}$, p and T are the velocity, pressure and temperature of the liquid, respectively. $\boldsymbol{g}$ is the acceleration due to gravity and $\nu = \mu/\rho$ is the kinematic viscosity of the liquid.

On the wall, we have the usual no-slip boundary condition

$$\boldsymbol{u} = 0 \quad \text{on } y = 0, \tag{2.2a}$$

while for the temperature boundary condition we have two types of boundary condition, namely, HF and ST as discussed in § 1. For HF, the thermal boundary condition is (Scheid 2004)

$$\text{HF: } \lambda \nabla T \cdot \boldsymbol{j} = -q_0 + \alpha_w (T - T_a) \quad \text{on } y = 0, \tag{2.2b}$$

where $\boldsymbol{j}$ is the unit vector normal to the wall and pointing into the liquid and α_w is the heat transfer coefficient of the wall–air interface. This mixed/Robin boundary condition implies that both the flux supplied by the solid substrate to the liquid q_0 and the heat losses $\alpha_w(T - T_a)$ to the ambient gas phase contribute to the temperature gradient at $y = 0$. On the other hand, for ST the thermal boundary condition is simply a Dirichlet one

$$\text{ST: } T = T_w \quad \text{on} \quad y = 0, \tag{2.2c}$$

and the heater is assumed to maintain the wall temperature at a constant value T_w. We note that since HF involves the heat flux from the wall to the substrate and the heat losses from the wall to the ambient gas phase, it is a more realistic condition than the ST one. In fact, experimental studies with locally heated falling films (Kabov 1998; Kabov *et al.* 2000) indicate that in practice it is almost impossible to maintain a constant temperature on the wall; instead it is a lot easier to control the heat flux (heat production). As a result, these studies suggest that most probably heated-film problems would require a mixed boundary condition. HF also allows for a non-uniformity of the heat flux along the plate owing to the non-uniformity of the plate temperature which in turn is due to the dependence of the plate temperature on the flow characteristics. Further, we note that, with the exception of Scheid (2004) all previous studies on heated films imposed the ST condition only.

On the interface, we have the kinematic boundary condition along with the normal and tangential stress balances

$$h_t + \boldsymbol{u} \cdot \nabla(h - y) = 0, \quad p_a + \boldsymbol{\tau} \cdot \boldsymbol{n} \cdot \boldsymbol{n} = -\sigma \nabla \cdot \boldsymbol{n}, \quad \boldsymbol{\tau} \cdot \boldsymbol{n} \cdot \boldsymbol{t} = \nabla \sigma \cdot \boldsymbol{t}, \tag{2.2d}$$

where $\boldsymbol{n}$ and $\boldsymbol{t}$ are unit vectors, normal (outward-pointing) and tangential to the interface, respectively, and $\boldsymbol{\tau} = -p\boldsymbol{I} + 2\mu\boldsymbol{e}$ is the stress tensor with $\boldsymbol{e}$ the rate-of-strain tensor given by $e_{ij} = (1/2)(\partial u_i/\partial x_j + \partial u_j/\partial x_i)$. p_a is the pressure of the ambient

https://doi.org/10.1017/S0022112007008476 Published online by Cambridge University Press

gas phase and σ is the surface tension. The thermal boundary condition on the free surface is:

$$\lambda \nabla T \cdot \boldsymbol{n} = -\alpha_g (T - T_a) \quad \text{on} \quad y = h, \tag{2.2e}$$

where α_g is the heat transfer coefficient between the liquid and air. Finally, the thermocapillary effect is modelled using a linear approximation for the surface tension

$$\sigma = \sigma_a - \gamma (T - T_a), \tag{2.3}$$

where σ_a is the surface tension at the temperature T_a and $\gamma > 0$ for typical liquids.

2.2. *Scalings and non-dimensionalization*

System (2.1)–(2.3) has a trivial solution corresponding to the plane-parallel base state, the Nusselt flat-film solution:

$$h = h_{\mathrm{N}}, \;\; p = p_a + \rho (h_{\mathrm{N}} - y) g \cos\beta, \;\; u = \frac{g \sin\beta}{2\nu} (2 h_{\mathrm{N}} y - y^2), \;\; v = 0, \tag{2.4a}$$

$$\mathrm{HF}: \; T = T_a + \beta_T [\lambda + \alpha_g (h_{\mathrm{N}} - y)], \quad \mathrm{ST}: \; T = T_a + \hat{\beta}_T [\lambda + \alpha_g (h_{\mathrm{N}} - y)], \tag{2.4b}$$

where $\beta_T = q_0 / [\lambda(\alpha_w + \alpha_g) + \alpha_w \alpha_g h_{\mathrm{N}}]$ and $\hat{\beta}_T = (T_w - T_a)/(\lambda + \alpha_g h_{\mathrm{N}})$. Using both the dimensional Nusselt film thickness, h_N, and the viscous-gravity length and time scales,

$$l_0 = \frac{\nu^{2/3}}{(g \sin\beta)^{1/3}}, \quad t_0 = \frac{\nu^{1/3}}{(g \sin\beta)^{2/3}},$$

we employ the non-dimensionalization

$$(\bar{x}, \bar{y}, \bar{h}) = \frac{(x, y, h)}{h_N}, \quad \bar{t} = \frac{t}{t_0 l_0 / h_N}, \quad (\bar{u}, \bar{v}) = \frac{(u, v)}{h_N^2 / t_0 l_0}, \quad \bar{p} = \frac{p - p_a}{\rho l_0 h_N / t_0^2},$$

$$\mathrm{HF}: \; \bar{T} = \frac{T - T_a}{q_0 h_N / \lambda}, \quad \mathrm{ST}: \; \bar{T} = \frac{T - T_a}{T_w - T_a}.$$

The temperature scales for HF and ST, $q_0 h_{\mathrm{N}}/\lambda$ and $T_w - T_a$, respectively, are natural control parameters in experiments.

In terms of these non-dimensional variables, the equations of motion and energy become

$$u_x + v_y = 0, \tag{2.5a}$$

$$3Re(u_t + u u_x + v u_y) = -p_x + u_{xx} + u_{yy} + 1, \tag{2.5b}$$

$$3Re(v_t + u v_x + v v_y) = -p_y + v_{xx} + v_{yy} - \cot\beta, \tag{2.5c}$$

$$3Pe(T_t + u T_x + v T_y) = T_{xx} + T_{yy}, \tag{2.5d}$$

where bars have been dropped for convenience. The wall boundary conditions become

$$u = v = 0, \quad \mathrm{HF}: \; T_y = -1 + B_w T, \quad \mathrm{ST}: \; T = 1, \tag{2.6a}$$

and the free-surface boundary conditions are written as

$$h_t + u h_x - v = 0, \tag{2.6b}$$

$$p + (We - MT) N^{-3/2} h_{xx} = 2N^{-1} (v_y - h_x (u_y + v_x) + h_x^2 u_x), \tag{2.6c}$$

$$u_y + M(T_x + h_x T_y) N^{1/2} = -v_x - 2h_x (v_y - u_x) + h_x^2 (u_y + v_x), \tag{2.6d}$$

$$T_y + BT N^{1/2} = h_x T_x, \tag{2.6e}$$

https://doi.org/10.1017/S0022112007008476 Published online by Cambridge University Press

where $N = 1 + h_x^2$. We now introduce the Kapitza, Marangoni, wall Biot and surface Biot numbers for HF, respectively,

$$Ka = \frac{\sigma_a}{\rho g l_0^2 \sin\beta}, \quad Ma = \frac{\gamma q_0}{\lambda \rho g l_0 \sin\beta}, \quad Bi_w = \frac{\alpha_w l_0}{\lambda}, \quad Bi = \frac{\alpha_g l_0}{\lambda},$$

and the Marangoni and surface Biot numbers for ST, respectively,

$$\hat{Ma} = \frac{\gamma(T_w - T_a)}{\rho g l_0^2 \sin\beta}, \quad \hat{Bi} = Bi,$$

where hats throughout this study are used to denote parameters associated with the ST problem. Further, we introduce the dimensionless Nusselt flat-film thickness, $\bar{h}_N = h_N/l_0$. The dimensionless groups in (2.5)–(2.6) can then be written as

$$Re = \frac{\bar{h}_N^3}{3}, \quad Pe = Re\,Pr, \quad We = \frac{Ka}{\bar{h}_N^2}, \quad M = \frac{Ma}{\bar{h}_N}, \quad B_w = Bi_w \bar{h}_N, \quad B = Bi\bar{h}_N, \tag{2.7}$$

corresponding to the Reynolds, Péclet, Weber numbers and the modified groups, Marangoni, wall Biot and surface Biot numbers for HF, respectively, and

$$\hat{M} = \frac{\hat{Ma}}{\bar{h}_N^2}, \quad \hat{B} = \hat{Bi}\bar{h}_N,$$

corresponding to the modified groups, Marangoni and surface Biot numbers for ST, respectively. $Pr = \nu/\kappa$ is the Prandtl number.

The set of dimensionless groups in (2.7) isolates the dependence on the dimensionless Nusselt flat-film thickness $\bar{h}_N$ and the physical properties of the problem. Hence, the system of equations (2.5)–(2.6) is governed by the inclination angle β, $\bar{h}_N$ or equivalently the Reynolds number and the five dimensionless parameters, Ka, Ma, Pr, Bi_w and Bi for HF and the four dimensionless groups, Ka, $\hat{Ma}$, Pr and $\hat{Bi}$ for ST. As a consequence, a complete investigation over the entire parameter space would be impractical. However, for a given liquid–gas system, heating conditions and geometry, the parameters β, Ka, Ma, Pr, Bi_w, Bi, $\hat{Ma}$ and $\hat{Bi}$ are fixed and the only free parameter is the Reynolds number which is a flow-control parameter so that the heated-falling-film problem is a one-parameter system only. On the other hand, if we fix only the liquid and inclination angle β, the Prandtl and Kapitza numbers are fixed, thus reducing the number of relevant parameters by three, which is a substantial simplification. As an example, assuming the liquid phase to be water at 25 °C and the plane to be vertical, $\beta = \pi/2$, $Ka \simeq 2850$ and $Pr \simeq 7$. The HF problem then has four free parameters, Re, Ma, Bi_w and Bi whereas the ST problem has three free parameters, Re, $\hat{Ma}$ and $\hat{Bi}$. The values for the parameters, Bi_w, Bi, Ma, $\hat{Bi}$ and $\hat{Ma}$ will be discussed in § 4.

2.3. *On the two wall thermal conditions: retrieving ST from HF*

We close this section with a comment on the wall thermal boundary condition for HF in (2.6*a*). The temperature field has been non-dimensionalized with $q_0 h_N/\lambda$. An alternative scaling could have been $T^* = (T - T_a)/(q_0/\alpha_w)$ which would convert (2.2*b*) to

$$T_y^* = B_w(T^* - 1). \tag{2.8}$$

In the limit $B_w \to \infty$, (2.8) yields $T^* \to 1$, thus retrieving the boundary condition for ST (2.6*a*); but (2.6*a*) is obtained by scaling the temperature field with $T_w - T_a$. This scaling must be related to that used to obtain (2.8) as in the limit $B_w \to \infty$, ST and HF are one and the same problem. Converting now $T^* = 1$ to dimensional variables

https://doi.org/10.1017/S0022112007008476 Published online by Cambridge University Press

and setting $T = T_w$ yields $q_0 = \alpha_w(T_w - T_a)$: q_0 is now the heat transported between the liquid and the gas. This is to be expected as, in the limit $B_w \to \infty$, the wall is effectively decoupled from the problem and we are concerned with the heat transfer between the liquid and the gas only.

Taking the limit $B_w \to \infty$ in (2.6*a*) yields $T \to 0$. It would then appear that we cannot retrieve the ST problem from (2.6*a*) in this limit. Note, however, that (2.6*a*) can be converted to (2.8) by using the transformation

$$T = \frac{1}{B_w} T^*. \tag{2.9}$$

Thus in the limit $B_w \to \infty$, $T^* \to 1$ becomes $T \to 0$ and hence, the alternative form of the wall thermal boundary condition in (2.8) is equivalent to (2.6). The 'advantage' of (2.8) is that it makes the recovery of ST from HF in the limit $B_w \to \infty$ transparent. On the other hand, the 'advantage' of (2.6*a*) is that it makes the limit $B_w \to 0$ more obvious as in this limit we retrieve the case of a specified heat flux boundary condition.

3. Linear stability analysis

3.1. *The Orr–Sommerfeld eigenvalue problem*

We now examine the linear stability of the Nusselt flat-film solution (2.4). For ST, this problem was first formulated and solved by Goussis & Kelly (1991) and reconsidered in detail by Scheid *et al.* (2005). The Nusselt solution can be written as

$$\overline{h} = 1, \quad \overline{v} = 0, \ \overline{u} = y - \tfrac{1}{2}y^2, \quad \overline{p} = (1-y)\cot\beta, \quad \overline{T} = [1 + B(1-y)]\overline{F},$$

where for ST $\overline{F} \to \overline{\hat{F}}$ with

$$\text{HF: } \overline{F} = (B_w + B + B_w B)^{-1}, \quad \text{ST: } \overline{\hat{F}} = (1 + \hat{B})^{-1}.$$

Normal form disturbances are introduced as

$$[h, u, v, p, T] = [\overline{h}, \overline{u}(y), \overline{v}(y), \overline{p}(y), \overline{T}(y)] + \chi \exp(\mathrm{i}k(x - ct))[H, \psi_y(y), -\mathrm{i}k\psi(y), \pi(y), \tau(y)],$$

where k and c are the wavenumber and complex phase velocity of the infinitesimal perturbations, respectively. The disturbances are substituted into (2.5) and (2.6) which are then linearized in χ. The pressure field is eliminated from the problem via the two momentum equations and the normal stress condition to yield the Orr–Sommerfeld eigenvalue problem

$$(\mathrm{D}^2 - k^2)^2\psi = 3\mathrm{i}kRe[\psi + (\overline{u} - c)(\mathrm{D}^2 - k^2)\psi], \tag{3.1a}$$

$$(\mathrm{D}^2 - k^2)\tau = 3\mathrm{i}kPe[B\overline{F}\psi + (\overline{u} - c)\tau], \tag{3.1b}$$

subject to the wall boundary conditions

$$\psi(0) = \mathrm{D}\psi(0) = 0, \quad \text{HF: } \mathrm{D}\tau(0) = B_w\tau(0), \quad \text{ST: } \tau(0) = 0, \tag{3.2a}$$

and the interfacial boundary conditions

$$\left[\mathrm{D}^2 - 3k^2 + 3\mathrm{i}kRe\left(c - \tfrac{1}{2}\right)\right]\mathrm{D}\psi(1) = \mathrm{i}k[\cot\beta + k^2(We - M\overline{F})]H, \tag{3.2b}$$

$$(\mathrm{D}^2 + k^2)\psi(1) = H + \mathrm{i}k\frac{M}{B}\mathrm{D}\tau(1), \tag{3.2c}$$

$$\mathrm{D}\tau(1) = B[B\overline{F}H - \tau(1)] \quad \text{with} \quad H = \frac{\psi(1)}{c - 1/2}, \tag{3.2d}$$

https://doi.org/10.1017/S0022112007008476 Published online by Cambridge University Press

where $\mathrm{D} \equiv \mathrm{d}/\mathrm{d}y$. For ST $(M, \overline{F}, B) \to (\hat{M}, \overline{\hat{F}}, \hat{B})$.

3.2. *Small wavenumber expansion*

Although a full solution to (3.1) and (3.2) can only be obtained numerically, an analytical solution can be obtained for $k \to 0$. As (3.1) and (3.2) are linear in τ and ψ and only odd powers of k have an imaginary coefficient, it is appropriate to seek a solution in the form

$$[\psi, \tau, c] = \frac{\mathrm{i}}{k}[\psi_{-1}, \tau_{-1}, c_{-1}] + [\psi_0, \tau_0, c_0] + \mathrm{i}k[\psi_1, \tau_1, c_1] + [O(k^2), O(k^2), O(k^2)].$$

Substituting these expansions into (3.1) and (3.2) and expanding in powers of k gives a sequential solution of the eigenvalue problem. The eigenvalue c is determined from the tangential stress balance (3.2*c*) where the Marangoni effect is predominant. The only root of the dispersion relation that can become unstable has a c for HF given by

$$\left.\begin{aligned} &c_{-1} = 0,\ \ c_0 = 1,\ \ c_1 = \tfrac{2}{5}Re - \tfrac{1}{3}\cot\beta + \tfrac{1}{2}MB_wB\overline{F}^2, \\ &c_2 = -1 - \tfrac{10}{7}Rec_1 + \frac{Re}{560}MB_wB\overline{F}^2 + \frac{Pe}{80}MB\overline{F}^3\left[60B + (35B-20)B_w + (7B-15)B_w^2\right], \end{aligned}\right\} \tag{3.4a}$$

and for ST given by

$$\left.\begin{aligned} &\hat{c}_{-1} = 0, \quad \hat{c}_0 = 1,\ \ \hat{c}_1 = \tfrac{2}{5}Re - \tfrac{1}{3}\cot\beta + \tfrac{1}{2}\hat{M}\hat{B}\overline{\hat{F}}^2, \\ &\hat{c}_2 = -1 - \tfrac{10}{7}Re\hat{c}_1 + \frac{Re}{560}\hat{M}\hat{B}\overline{\hat{F}}^2 + \frac{Pe}{80}\hat{M}\hat{B}\overline{\hat{F}}^3(7\hat{B} - 15). \end{aligned}\right\} \tag{3.4b}$$

There are also an infinite number of stable eigenvalues whose leading-order terms in the absence of the Marangoni effect assume the simple form $-4in^2\pi^2/(3Re\,k)$ where n is an integer. These are the shear modes associated with the semi-parabolic Nusselt profile (see e.g. Chang & Demekhin 2002).

3.3. *Critical conditions*

The onset of the instability occurs at $c_1 = 0$ which yields the critical conditions

$$\mathrm{HF}: Re_c = \tfrac{5}{6}\cot\beta - \tfrac{5}{4}MB_wB\overline{F}^2, \tag{3.5a}$$

$$\mathrm{ST}: Re_c = \tfrac{5}{6}\cot\beta - \tfrac{5}{4}\hat{M}\hat{B}\overline{\hat{F}}^2, \tag{3.5b}$$

for the critical Reynolds number Re_c above which the flow loses stability. These conditions establish that for $M, \hat{M} > 0$, the Marangoni effect is destabilizing as Re_c decreases with increasing $M, \hat{M}$. The situation is reversed when $M, \hat{M} < 0$. Finally, note that for $M = \hat{M} = 0$, the above expressions reduce to the well-known critical condition for a free-falling film, $Re_c = (5/6)\cot\beta$ (Benjamin 1957; Yih 1963). Note that if the wall is perfectly insulated from the air, i.e. $B_w = 0$ in which case we have a specified heat flux condition, $Re_c = (5/6)\cot\beta$ and the Marangoni effect does not influence the instability onset. We shall return to this point in the next section.

https://doi.org/10.1017/S0022112007008476 Published online by Cambridge University Press

4. Long-wave theory for large Péclet numbers

4.1. *Derivation of free-surface evolution equations: LWE-HF and LWE-ST models*

By introducing a formal parameter ϵ representing a typical slope of the film, we can perform a gradient expansion $\partial_{x,t} \sim \epsilon \ll 1$ as initially performed by Benney (1966) for the isothermal case. A classical Benney expansion assumes all parameters are $O(1)$, with the exception of the Weber number which is taken to be much larger. The Reynolds number, Marangoni number and wall/free-surface Biot numbers are then assumed to be $O(1)$. The Weber number is assumed to be $O(\epsilon^{-2})$, to bring the dominant surface tension effects in at $O(\epsilon)$. These stabilizing terms prevent the waves from forming shocks and from breaking, thus satisfying the long-wave approximation. With regard to the Péclet number, all previous LWE theories in the area of heated thin films, e.g. Joo *et al.* (1991) and Oron *et al.* (1997), have assumed the Péclet number to be $O(1)$. As a consequence, the convective heat transport effects only enter the velocity field at $O(\epsilon^2)$ and temperature field at $O(\epsilon)$, but these higher-order corrections are rather lengthy, leading in turn to lengthy evolution equations for the free surface.

In practice, however, the Péclet number can be much larger than the Reynolds number owing to the ratio of the momentum and thermal diffusivities being much larger than unity – note that for water $Pr = 7$. We then expect that convection at large Péclet numbers can lead to a downstream convective distortion of the free-surface temperature distribution obtained by assuming an $O(1)$ Péclet number. As a result, the transport of heat by the flow becomes important and can significantly modify the interfacial temperature and consequently the Marangoni effect on the fluid flow. Hence we assume $Pe \sim O(\epsilon^{-n})$ with $0 < n < 1$ so that the convective heat transport effects are included at a low relevant order. If $Pe = O(1)$, then for the level of truncation employed here the convective heat transport effects would be neglected and as noted earlier we would have to go up to $O(\epsilon^2)$ and $O(\epsilon)$ for the velocity and temperature fields, respectively.

We then carry out an expansion for the velocity up to $O(\epsilon^{2-n})$ and we neglect terms of $O(\epsilon^2)$ and higher. This level of truncation allows the derivation of a relatively simple evolution equation for the local film thickness. The pressure and temperature are both expanded up to $O(\epsilon^{1-n})$ and hence terms of $O(\epsilon)$ and higher are omitted from these expansions. At this level of truncation, the solutions for the temperature field are given by equation (A 1) in Appendix A. The velocity components can be conveniently expressed in the form $u = \psi_y$ and $v = -\psi_x$ where the streamfunction ψ is given by (A 2). The free-surface evolution equation can then be obtained easily from the kinematic boundary condition in (2.6*b*):

$$\text{HF: } h_t + h^2 h_x + \left(\tfrac{2}{5} Re h^6 h_x - \tfrac{1}{3} h^3 h_x \cot\beta + \tfrac{1}{2} MB_w BF^2 h^2 h_x + \tfrac{1}{3} We h^3 h_{xxx}\right)_x - \frac{Pe}{80} MB \left[h^2 \left(G h^3 h_x\right)_x\right]_x = 0, \quad (4.1)$$

with the functions F and G being given in Appendix A. The equivalent evolution equation for the ST problem is obtained with $(G, MB_w BF^2, MB) \to (\hat{G}, \hat{M}\hat{B}\hat{F}^2, \hat{M}\hat{B})$.

A linear stability analysis of the trivial solution $h = 1$ of (4.1) and the equivalent evolution equation for ST gives the same critical conditions as (3.5) obtained from the Orr–Sommerfeld eigenvalue problem of the full Navier–Stokes and energy equations. This is to be expected as LWE is exact regarding critical/neutral conditions, as pointed out in § 1.1. However, LWE being a single equation predicts only the mode that becomes unstable and fails to recover the stable modes obtained with Orr–Sommerfeld,

https://doi.org/10.1017/S0022112007008476 Published online by Cambridge University Press

a consequence of the fact that in LWE these modes are slaved to h (these modes have their own intrinsic dynamics and can be destabilized for very large Re).

4.1.1. *Physical consequences of vanishing wall/free-surface Biot numbers*

When $B_w = 0$, the fifth term in (4.1) vanishes and the Marangoni effect no longer influences the instability onset. This means that for a specified heat flux boundary condition or equivalently a plate that is perfectly insulated from the gas phase below, the long-wave thermocapillary instability is suppressed. In this case, the interfacial temperature distribution is $T|_{y=h} = B^{-1} + (3/2)PeB^{-1}h^3h_x$ which has two contributions: B^{-1} due to heat conduction across the film and $(3/2)PeB^{-1}h^3h_x$ due to convective heat transport. The first term is independent of h and, as a result, thermocapillarity does not affect the instability as variations of h do not induce perturbations on the interfacial temperature distribution through heat conduction. The second term of $T|_{y=h}$ due to heat convection does depend on h and controls the dispersion of the waves through the last term in (4.1) (via the functionals G, $\hat{G}$). Hence, enabling heat losses at the wall through the mixed boundary condition (2.6a) is the only way to enable the Marangoni instability (unless the wall supplies a non-uniform heat flux (e.g. Scheid *et al.* 2002).

On the other hand, for the ST problem the interfacial temperature distribution is $T|_{y=h} = (1+\hat{B}h)^{-1} + (1/40)Pe\hat{B}\hat{G}h^3h_x$. The first term arises from heat conduction and depends on h so that the Marangoni forces in this case always influence the instability onset, as long as $\hat{B} \neq 0$. However, if $\hat{B} = 0$, i.e. the interface is a poor heat conductor perfectly insulated from the surrounding gas, the Marangoni effect does not influence the system. In this case $T = 1$ from (A 1b) and the temperature is everywhere uniform and equal to the wall temperature so that there is no instability due to the thermal effects or influence on the dispersion of the waves; the momentum and heat transport problems are decoupled in this limit.

4.2. *Rescaling the LWE equations*

For convenience, let us now rescale the evolution equations using the scalings introduced by Shkadov (1977). He introduced a length scale in the streamwise direction corresponding to the balance of the pressure gradient $\sigma_a h_{xxx}$ due to surface tension and the acceleration due to gravity $\rho g \sin\beta$. This length scale, say l_S, corresponds effectively to the characteristic length of the steep front of the waves. Note that l_S should be much larger than the film thickness h_N in order to sustain the long-wave assumption. Simple algebra then shows that $l_S/h_N = We^{1/3}$ which is a large ratio as long as the Weber number is sufficiently large. The rescaled space and time coordinates are then defined as $x = We^{1/3}X$ and $t = We^{1/3}\Theta$ to yield

$$\mathrm{HF}:\ h_\Theta + h^2h_X + \left(\mathscr{A}(h)h_X + \mathscr{B}(h)h_X^2 + \mathscr{C}(h)h_{XX} + \tfrac{1}{3}h^3h_{XXX}\right)_X = 0, \qquad (4.2)$$

where

$$\mathscr{A}(h) = \frac{2\delta}{15}h^6 - \frac{\zeta}{3}h^3 + \frac{\mathscr{M}}{2}B_wBF^2h^2, \quad \mathscr{B}(h) = h^2\frac{\partial}{\partial h}\left(\frac{\mathscr{C}(h)}{h^2}\right), \quad \mathscr{C}(h) = -\frac{Pr\delta}{240}\mathscr{M}BGh^5.$$

For ST, $\hat{\mathscr{A}}$ is obtained from $\mathscr{A}$ with $\mathscr{M}B_wBF^2 \to \hat{\mathscr{M}}\hat{B}\hat{F}^2$ and $\hat{\mathscr{C}}$ is obtained from $\hat{\mathscr{C}}$ with $\mathscr{M}BG \to \hat{\mathscr{M}}\hat{B}\hat{G}$. The parameters

$$\delta = 3Re/We^{1/3}, \quad \zeta = \cot\beta/We^{1/3}, \quad \mathscr{M} = M/We^{1/3}, \quad \hat{\mathscr{M}} = \hat{M}/We^{1/3}$$

are reduced Reynolds number, reduced slope and reduced Marangoni numbers.

In what follows, the evolution equation (4.2) will be referred to as LWE-HF and the corresponding equation for ST as LWE-ST. The LWE models are developed to verify

https://doi.org/10.1017/S0022112007008476 Published online by Cambridge University Press

the behaviour of the weighted residuals models obtained in the following sections in the region where LWE is valid, i.e. close to criticality. It is exactly because of the presence of convective heat transport terms in the weighted residuals models to be developed, that we have developed a long-wave theory to include these terms.

4.3. *Comparing HF and ST*

4.3.1. *Conditions under which HF and ST are identical*

Despite the different wall boundary conditions, the HF and ST problems yield similar Marangoni terms in their respective long-wave evolution equations. As discussed earlier, the leading-order Marangoni effects arise via heat conduction and the higher-order Marangoni effects via heat convection. By comparing (4.1) for the HF problem to its counterpart for the ST problem, it is clear that the leading-order Marangoni terms in these two equations, also responsible for the thermocapillary instability, are identical when $MB_wBF^2 = \hat{M}\hat{B}\hat{F}^2$. This relationship can be made independent of h when the following two conditions are satisfied:

$$\hat{B} = \frac{B_w B}{B_w + B}, \quad \hat{M} = \frac{M}{B_w + B}.$$

By eliminating the film parameter $\bar{h}_N$, the above conditions can be written as

$$\hat{Bi} = \frac{Bi_w Bi}{Bi_w + Bi}, \quad \hat{Ma} = \frac{Ma}{Bi_w + Bi}. \tag{4.3}$$

In this case, the critical Reynolds numbers given in (3.5*a*) and (3.5*b*) become identical. This shows that the Marangoni effects associated with the HF and ST problems are identical at least in the long-wave limit and provided that the convective effects can be neglected, i.e. small Pe. Away from the small Pe limit, the criticality conditions are the same, but the phase velocities of the infinitesimal disturbances are different – recall that the convective heat transport effects influence the dispersion of the waves. The two cases will also be different in the nonlinear stage of the instability.

4.3.2. *On the type of small-amplitude waves*

The LWE equation obtained by Trevelyan & Kalliadasis (2004*a*) in their study of the dynamics of a reactive falling film is the same as that in (4.2) but with $\mathscr{A}$, $\mathscr{B}$ and $\mathscr{C}$ different polynomial functions of h. Hence, the results of Trevelyan & Kalliadasis (2004*a*) can be easily extended to (4.2), and for that matter to any evolution equation of the type given in (4.2) where $\mathscr{A}$, $\mathscr{B}$ and $\mathscr{C}$ are some polynomial functions of h. In particular, as these authors demonstrated, for evolution equations of the type given in (4.2), we can have both positive and negative stationary solitary-wave solutions at the weakly nonlinear stage, but one of them is unstable in time-dependent computations. More specifically, when $\overline{\mathscr{C}}$ is sufficiently large and positive (the bar denotes evaluation of the function $\mathscr{C}$ at $h = 1$), time-dependent computations show that the system evolves into a train of positive-hump solitary waves. Such waves travel with a speed faster than the linear wave speed and their largest free-surface deformation is away from the wall. On the other hand, when $\overline{\mathscr{C}}$ is sufficiently large and negative, the system evolves into a train of negative-hump waves which travel with speed smaller than the linear wave speed and with the largest free-surface deformation towards the wall. We note that although $\overline{\mathscr{C}}$ determines the type of wave (positive or negative), it is the full term $\overline{\mathscr{C}}h_{xxx}$ that governs the dispersion of small-amplitude waves.

The sign of $\overline{\mathscr{C}}$ is opposite to that of the convective functions G and $\hat{G}$. In the limit of very thin films, i.e. $\bar{h}_N \to 0$, the signs of the convective functions G in Appendix A

https://doi.org/10.1017/S0022112007008476 Published online by Cambridge University Press

determine that for ST $\overline{\hat{\mathscr{C}}} > 0$, whilst for HF $\overline{\mathscr{C}}$ is only positive when $Bi_w/Bi > 3$. Thus, in the ST case we always have positive-hump solitary waves, whilst in the HF case we can have either positive- or negative-hump solitary waves. We note that in the limit of zero $\bar{h}_{\mathrm{N}}$, the Reynolds number tends to zero and the critical Reynolds number tends to minus infinity which is of course unphysical and implies a zero critical Reynolds number. Nevertheless, we refrain from using the expression 'close to criticality' in this limit as in general it implies small-amplitude waves. Obviously, close to criticality, i.e. for a finite value of Re_c, the dispersive effects of the (small-amplitude) waves in LWE are controlled by $\overline{\mathscr{C}} h_{xxx}$.

4.3.3. *Choosing parameter values to contrast HF and ST*

In order to contrast now the ST and HF problems, we shall apply both conditions in (4.3). The first condition in (4.3) requires that both Bi and Bi_w are greater than $\hat{Bi}$. It is realistic to expect poor heat transfer characteristics at the liquid–gas interface and so physically the parameters Bi and $\hat{Bi}$ should be small. For the surface Biot number we take $\hat{Bi} = 1/10$ for ST throughout this study. By rearranging now the conditions in (4.3), we obtain $Bi = Bi_w \hat{Bi}/(Bi_w - \hat{Bi})$ and $Ma = \hat{Ma} Bi_w^2/(Bi_w - \hat{Bi})$. We then consider two sets of parameter values for HF, namely,

$$[Bi_w, Bi, Ma] = \left[\tfrac{1}{5}, \tfrac{1}{5}, \tfrac{2}{5}\hat{Ma}\right], \quad [Bi_w, Bi, Ma] = \left[\tfrac{3}{5}, \tfrac{3}{25}, \tfrac{18}{25}\hat{Ma}\right].$$

For the first set of parameters $Bi_w/Bi = 1$, whilst for the second set $Bi_w/Bi = 5$, the two ratios being equidistant from 3. The first set yields $\mathscr{C} < 0$ for small $\bar{h}_{\mathrm{N}}$, whilst the second set yields $\mathscr{C} > 0$ for small $\bar{h}_{\mathrm{N}}$ and we expect that the second set will yield qualitative agreement (at least for small Re) with the ST problem which always has $\hat{\mathscr{C}} > 0$ for small $\bar{h}_{\mathrm{N}}$.

The only free parameters then are $\hat{Ma}$ and Re – see also our discussion in § 2.2.

5. Weighted residuals approach

5.1. *The momentum equation*

The starting point of the weighted residuals approach is to assume long waves in the streamwise direction. For consistency with LWE, we shall also neglect the second-order diffusive terms u_{xx} and T_{xx} of the Navier–Stokes and energy equations. Part of the analysis presented in this section parallels the works by Kalliadasis *et al.* (2003*a*, *b*) and the reader is referred to these studies for further details. The second-order terms can be included with the methodology developed by Ruyer-Quil *et al.* (2005).

To leading order, the y-component of the equation of motion (2.5*c*) and normal stress balance (2.6*c*) are $p_y = -\cot\beta$ and $p|_{y=h} = -We h_{xx}$. Hence, the pressure distribution is given by $p = (h - y)\cot\beta - We h_{xx}$ which when substituted into the x-component of the momentum equation (2.5*b*) and neglecting terms of $O(\epsilon^2)$ and higher yields

$$u_{yy} + 1 = h_x \cot\beta - We h_{xxx} + 3Re(u_t + u u_x + v u_y). \tag{5.1a}$$

The y-component of the velocity can be eliminated by using the continuity equation (2.5a) along with the no-slip boundary condition to obtain $v = -\int_0^y u_x \, \mathrm{d}y'$. The u velocity must satisfy the no-slip boundary condition and the leading-order tangential stress balance on the interface from (2.6*d*),

$$u = 0 \quad \text{on} \quad y = 0, \quad u_y = -M\theta_x \quad \text{on} \quad y = h, \tag{5.1b}$$

https://doi.org/10.1017/S0022112007008476 Published online by Cambridge University Press

where terms of $O(\epsilon^2)$ and higher have been neglected from the tangential stress balance and $\theta(x,t)$ is the interfacial temperature, i.e. $\theta \equiv T|_{y=h}$ and $\theta_x \equiv (T_x + h_x T_y)|_{y=h}$. The above system is coupled with the energy equation and thermal boundary conditions, however, we can examine the flow field by assuming that the function θ is known. The system is then closed via the kinematic boundary condition in (2.6), which by integrating the continuity equation in (2.5) across the film can be written as

$$h_t + q_x = 0, \tag{5.1c}$$

where $q = \int_0^h u\,\mathrm{d}y$ is the flow rate. In the absence of the Marangoni term $M\theta_x$ appearing in the stress balance at the free surface, equations (5.1) are the so-called 'boundary-layer equations'.

Following Kalliadasis *et al.* (2003*a*, *b*) we assume the following velocity profile,

$$u = 3\frac{q}{h}\left(\eta - \tfrac{1}{2}\eta^2\right) + M\theta_x h\left(\tfrac{1}{2}\eta - \tfrac{3}{4}\eta^2\right) \equiv u^{(0)} + M\theta_x h\left(\tfrac{1}{2}\eta - \tfrac{3}{4}\eta^2\right), \tag{5.2}$$

where $\eta = y/h(x,t)$ is a reduced normal coordinate. $u^{(0)}$ is the test function that contains q for which an equation is sought that would provide a closure for the weighted residuals approach (it is identical to the test function introduced by Shkadov (1967, 1968) for isothermal flows). The second function is chosen so that the profile in (5.2) satisfies all boundary conditions (in fact it is the simplest possible profile that does so). The introduction of this profile into (5.1*a*) yields the following residual at $O(\epsilon)$:

$$R_u = 3Re\left(u_t^{(0)} + u^{(0)}u_x^{(0)} + v^{(0)}u_y^{(0)}\right) - u_{yy} - 1 + h_x\cot\beta - Weh_{xxx}, \tag{5.3}$$

where $v^{(0)} = -\int_0^y u_x^{(0)}\,\mathrm{d}y'$. Indeed, the Marangoni terms in (5.2) are $O(\epsilon M)$ so that they contribute only to the viscous diffusion term $\partial^2/\partial y^2$ and are neglected from the inertial terms which are $O(\epsilon Re)$.

For the isothermal falling-film problem, Ruyer-Quil & Manneville (2000, 2002) showed that a Galerkin projection for the velocity field with just one test function, the profile assumed by Shkadov (1967, 1968), and with a weight function equal to the test function itself fully corrects the critical Reynolds number obtained from the Shkadov IBL approximation. We shall demonstrate that this is also the case in the presence of Marangoni effects when the weight function is taken as the test function for the velocity, namely $\eta - \eta^2/2$. The momentum residual is then minimized from $\langle \eta - \eta^2/2, R_u\rangle = 0$ – the inner product is defined as $\langle f, g\rangle = \int_0^1 fg\,\mathrm{d}\eta$ for any two functions f and g with appropriate boundary conditions – which yields the averaged momentum equation

$$\frac{18}{5}Re\left(q_t + \frac{17}{7}\frac{q}{h}q_x - \frac{9}{7}\frac{q^2}{h^2}h_x\right) + \frac{3q}{h^2} = h + Wehh_{xxx} - hh_x\cot\beta - \frac{3}{2}M\theta_x, \tag{5.4}$$

used in the remainder of the study. Note that (5.1*c*) and (5.4) correspond to (5.17*a*) and (5.17*b*) in Scheid (2004) (and (4.18*a*) and (4.18*b*) in Ruyer-Quil *et al.* 2005).

Ruyer-Quil & Manneville (2000, 2002) also developed high-order IBL models using refined polynomial expansions for the velocity field (corresponding to corrections of the Shkadov parabolic self-similar profile) and high-order weighted residuals techniques. Here we leave the momentum equation as simple as possible and we aim to improve the treatment of the energy equation.

https://doi.org/10.1017/S0022112007008476 Published online by Cambridge University Press

5.2. *Simple weighted residuals for the energy equation: the SHF and SST models*

5.2.1. *Derivation of the models*

The boundary conditions for the temperature field are the wall conditions in (2.6*a*) and the leading-order interfacial condition from (2.6*e*)

$$T_y = -BT \quad \text{on} \quad y = h, \tag{5.5}$$

where terms of $O(\epsilon^2)$ and higher have been neglected. As with the averaging of the momentum equation, the first step in modelling the energy equation is the introduction of a test function for the temperature field. As a first approximation we choose a linear profile which satisfies the wall boundary condition in (2.6*a*) along with $T|_{\eta=1} = \theta$:

$$\text{HF: } T = \theta + \frac{1 - B_w\theta}{1 + B_w h} h(1 - \eta), \quad \text{ST: } T = 1 + (\theta - 1)\eta. \tag{5.6}$$

Hence, the assumption here is that the linear temperature profile obtained for a flat film persists even when the interface is no longer flat. Note that θ_x occurs explicitly in the momentum equation (5.4) and so it is convenient to explicitly include θ in the temperature fields.

By analogy now with our analysis for the momentum equation, the introduction of the above test functions for the temperature fields into (2.5*d*) yields the following residual at $O(\epsilon)$:

$$R_T = 3Pe\left(T_t + u^{(0)}T_x + v^{(0)}T_y\right) - T_{yy}, \tag{5.7}$$

where the $O(\epsilon M)$ terms of u and v are neglected from the heat transport convective terms which are $O(\epsilon Pe)$. The energy residual can then be minimized from $\langle w_T, R_T\rangle = 0$ where w_T is an appropriately chosen weight function.

We note that although the temperature distributions in (5.6) satisfy their respective wall boundary conditions in (2.6*a*), they do not satisfy the leading-order interfacial condition in (5.5), unlike the velocity profile in (5.2) which satisfies all boundary conditions. It is in fact impossible for a linear profile to satisfy (5.5) and $\langle w_T, R_T\rangle = 0$ however, as was pointed out by Kalliadasis *et al.* (2003*a*) by choosing the weight function appropriately, the boundary terms resulting from integrations by parts involve either T_η on $\eta = 1$ or T on $\eta = 0$ and thus the interfacial boundary condition can be included in the boundary terms resulting from the integrations by parts. Hence, although the test function does not satisfy all boundary conditions, the averaged energy equation does and the flat film solution can still be retained in our averaging formulation.

For HF we take $w_T \equiv 1$ which gives

$$0 = \frac{2 + B_w h}{2}\theta_t + \frac{8 + 5B_w h}{8h} q\theta_x - \frac{(1 - B_w\theta)}{8(1 + B_w h)}\left[(5 + B_w h)q_x - 3\frac{q h_x}{h}\right] + \frac{\theta F^{-1} - 1}{3Peh}. \tag{5.8a}$$

Equations (5.4) and (5.8*a*) along with the kinematic boundary condition in (5.1*c*) will be referred to hereinafter as the SHF model – a simple heat flux model. For ST we take $w_T \equiv y$ which gives

$$0 = \theta_t + \frac{27q}{20h}\theta_x + \frac{7q_x(\theta - 1)}{40h} + \frac{1}{Peh^2}(\theta\hat{F}^{-1} - 1). \tag{5.8b}$$

https://doi.org/10.1017/S0022112007008476 Published online by Cambridge University Press

Equations (5.4) and (5.8*b*) along with the kinematic boundary condition in (5.1*c*) will be referred to hereinafter as the SST model – a simple specified temperature model. Equations (5.8*a*) and (5.8*b*) correspond to (8.8) and (5.17*c*) in Scheid (2004). Equation (5.8*b*) also corresponds to (4.18*c*) in Ruyer-Quil *et al.* (2005).

For consistency the SHF and SST models are both rescaled in the same way as the LWE-HF and LWE-ST, i.e. $x = We^{1/3}X$ and $t = We^{1/3}\Theta$. Finally, we note that although the SST model essentially uses the test function as the weight function, we refrain from calling this model a 'Galerkin approach'. Indeed with a linear test function $T_{yy} \equiv 0$ and as pointed out earlier, SST satisfies the boundary conditions through integrations by parts.

5.2.2. *Linear stability of flat-film solution for the SHF and SST models*

By construction, the SHF and SST models satisfy their appropriate flat-film solutions, namely

$$h = 1, \quad q = \tfrac{1}{3}, \quad \text{HF: } \theta = \overline{F}, \quad \text{ST: } \theta = \overline{\hat{F}}.$$

We consider the stability of these solutions with respect to infinitesimal perturbations in the form of normal modes $\sim e^{ik(X-c\Theta)}$ where k and c are the wavenumber and complex phase velocity of the perturbations, respectively. Substituting these modes into the SHF/SST models linearized about their flat-film solutions gives the dispersion relation for ω as a function of k with three roots for c.

To obtain the critical condition for the onset of instability we consider $k \ll 1$ and expand the phase velocity as $c \sim (i/k)c_{-1} + c_0 + ikc_1 + k^2c_2 + O(k^3)$ (see also § 3.2). Two of the roots have $c_{-1} < 0$ and the corresponding modes are stable (note $\omega_R = \mathrm{Re}(-ikc) = c_{-1} + k^2c_1 + O(k^4)$ for small k). The third root can have a positive growth rate. For the SHF model the first few orders of the wave speed for this mode are given by,

$$\left.\begin{aligned} &c_{-1} = 0, \quad c_0 = 1, \quad c_1 = \frac{2\delta}{15} - \frac{\zeta}{3} + \frac{1}{2}\mathscr{M}B_wB\overline{F}^2, \\ &c_2 = \left(\frac{B}{4} - \frac{B_w}{12} + \frac{B_wB}{16}\right)(1+B_w)Pr\,\delta\mathscr{M}B\overline{F}^3 - \frac{10}{21}\delta c_1. \end{aligned}\right\} \tag{5.9a}$$

For the SST model we also have two roots with $\hat{c}_{-1} < 0$. The first few orders of the wave speed of the third mode that can become unstable are given by

$$\left.\begin{aligned} &\hat{c}_{-1} = 0, \quad \hat{c}_0 = 1, \quad \hat{c}_1 = \frac{2\delta}{15} - \frac{\zeta}{3} + \frac{1}{2}\hat{\mathscr{M}}\hat{B}\overline{\hat{F}}^2 \\ &\hat{c}_2 = (7\hat{B} - 15)\frac{Pr\,\delta}{240}\hat{\mathscr{M}}\hat{B}\overline{\hat{F}}^3 - \frac{10}{21}\delta\hat{c}_1. \end{aligned}\right\} \tag{5.9b}$$

The onset of the instability occurs at $c_1 = 0$ for SHF and $\hat{c}_1 = 0$ for SST which yields the same critical Reynods number with LHE-HF and LWE-ST which in turn is the same to that predicted from the Orr–Sommerfeld analysis – see (3.5). Regarding the linear wave speed, the Orr–Sommerfeld analysis in § 3.2 (with the wavenumber k scaled with $1/We^{1/3}$), LWE and SHF/SST all give the same values for c_0, c_1, $\hat{c}_0$ and $\hat{c}_1$ but not for c_2 and $\hat{c}_2$; agreement for c_2 and $\hat{c}_2$ would require taking into account for both LWE and SHF/SST the second-order dissipative terms which have been neglected here. Note that unlike Orr–Sommerfeld, for the weighted residuals models we have a finite number of modes due to their polynomial dispersion relation as a result of projection of the original equations onto a finite number of test functions (clearly, increasing the number of test functions would increase the number of modes).

https://doi.org/10.1017/S0022112007008476 Published online by Cambridge University Press

Finally, the neutral stability curve is obtained from $c_I = 0$. In general this has to be solved numerically, however, by taking the limit of small $\bar{h}_{\rm N}$ an analytical solution is possible. This gives $c_R = 1$ where

$$\text{HF: } k = \frac{\bar{h}_{\rm N}^{-1/6}}{B + B_w}\sqrt{\frac{3MBB_w}{2Ka^{1/3}}}\left[1 - \bar{h}_{\rm N}\left(\frac{BB_w}{B + B_w} + \frac{(B + B_w)^2\cot\beta}{3MBB_w}\right)\right] + O\left(\bar{h}_{\rm N}^{11/6}\right)$$

$$\text{ST: } k = \bar{h}_{\rm N}^{-1/6}\sqrt{\frac{3\hat{M}\hat{B}}{2Ka^{1/3}}}\left[1 - \bar{h}_{\rm N}\left(\hat{B} + \frac{\cot\beta}{3\hat{M}\hat{B}}\right)\right] + O\left(\bar{h}_{\rm N}^{11/6}\right).$$

Hence, the neutral wavenumber k for both HF and ST tends to infinity as $\bar{h}_{\rm N}$ tends to zero. Recall from § 4.3.2 that in this limit the Reynolds number tends to zero and the critical Reynolds number tends to minus infinity which is of course unphysical and implies a zero critical Reynolds number. Notice that by using condition (4.3), the above expressions for the HF and ST neutral wavenumbers are identical. This is to be expected since convection does not enter the above expansions in $\bar{h}_{\rm N}$ at the level of truncation for these expansions. Notice also that these expansions are not valid for $M = 0$. In this case an expansion for small $\bar{h}_{\rm N}$ is not necessary since we have the exact solution,

$$c_R = 1, \quad k = We^{-1/6}\sqrt{\tfrac{6}{5}Re - \cot\beta} \equiv We^{-1/6}\sqrt{\tfrac{6}{5}(Re - Re_c)},$$

which is identical to the LWE neutral stability curve in the absence of the Marangoni effect as can be easily shown from (4.1).

5.3. *Galerkin residuals of the energy equation: the GHF[m] and GST[m] models*

5.3.1. *Derivation of the models*

The simple weighted residuals models SHF and SST are useful prototypes for the study of the dynamics of a heated film. Also, the linear stability analysis of these models in § 5.2.2 showed that they do predict the correct critical Reynolds number. However, we also wish to recover close to criticality the LWE models obtained in § 4.

A more refined treatment of the temperature field will enable a weighted residuals approach to yield LWE via an appropriate gradient expansion. We consider a general polynomial expansion for the temperature field in powers of η and with amplitudes that are only functions of x and t:

$$\text{HF: } T = \sum_{i=-1}^{m} A^{(i)}(x,t)\eta^{i+1}, \quad \text{ST: } T = \sum_{i=-2}^{m} A^{(i)}(x,t)\eta^{i+2}.$$

We note that unlike the studies by Scheid (2004) and Ruyer-Quil *et al.* (2005) where the amplitudes in the expansion for the temperature field are assigned certain orders with respect to ϵ, in our projection for the temperature field the order of the amplitudes is not specified. We also note that the test functions used by Scheid (2004) and Ruyer-Quil *et al.* (2005) did not satisfy all boundary conditions; instead the weight functions were chosen so that the boundary conditions can be included in the boundary terms resulting from the integrations by parts as was done in § 5.2.1.

Here we require that the temperature field satisfies all of its boundary conditions along with $T|_{\eta=1} = \theta$, a total of three conditions that must be satisfied. For the HF problem then we eliminate a total of three amplitudes, $A^{(-1)}$, $A^{(0)}$ and $A^{(1)}$. For the ST problem we also use the condition $T_{yy} = 0$ on the wall which originates from a Taylor series expansion of the energy equation (2.5*d*) at $y = 0$ (this is also consistent with LWE-ST – T in (A 1*b*) has no quadratic term in y) and hence we eliminate four

https://doi.org/10.1017/S0022112007008476 Published online by Cambridge University Press

amplitudes, $A^{(-2)}$, $A^{(-1)}$, $A^{(0)}(\equiv 0)$ and $A^{(1)}$. In weighted residuals terminology, the elimination of these amplitudes for the HF and ST problems is effectively equivalent to a 'tau' method (Gottlieb & Orszag 1977).

We then project the temperature field onto the new set of test functions ϕ,

$$\text{HF: } T = \phi_0 + \theta\phi_1 + \sum_{i=2}^{m} A^{(i)}(x,t)\phi_i, \quad \text{ST: } T = \hat{\phi}_0 + \theta\hat{\phi}_1 + \sum_{i=2}^{m} A^{(i)}(x,t)\hat{\phi}_i, \tag{5.10}$$

where we now have m amplitude functions, θ, $A^{(2)}\ldots A^{(m)}$ and the test functions are defined by

$$\phi_0 = \frac{h(1-\eta)^2}{2+B_w h}, \quad \phi_1 = 1 + (1-\eta)\eta Bh + \phi_0(B - B_w),$$
$$\phi_i = \eta^{i+1} - (i+1)\frac{\eta^2}{2} + \frac{(i-1)(2+(2-\eta)\eta B_w h)}{2(2+B_w h)} \quad \text{for} \quad 2 \leqslant i \leqslant m,$$

and

$$\hat{\phi}_0 = 1 - \frac{3\eta}{2} + \frac{\eta^3}{2}, \quad \hat{\phi}_1 = 1 - \hat{\phi}_0 + \hat{B}h(1-\eta^2)\frac{\eta}{2},$$
$$\hat{\phi}_i = (i-1)\frac{\eta}{2} - (i+1)\frac{\eta^3}{2} + \eta^{i+2} \quad \text{for} \quad 2 \leqslant i \leqslant m.$$

All ϕ_i and $\hat{\phi}_i$ are non-negative in the open interval $(0,1)$. Also, by construction ϕ_i and $\hat{\phi}_i$ satisfy the same conditions on the surface, namely, $\phi_0 = \hat{\phi}_0 = \phi_1 - 1 = \hat{\phi}_1 - 1 = \phi_i = \hat{\phi}_i = 0$ and $\phi_{0_\eta} = \hat{\phi}_{0_\eta} = \phi_{1_\eta} + Bh = \hat{\phi}_{1_\eta} + \hat{B}h = \phi_{i_\eta} = \hat{\phi}_{i_\eta} = 0$. On the wall, ϕ_i satisfy $\phi_{0_\eta} + h - B_w h\phi_0 = \phi_{1_\eta} - B_w h\phi_1 = \phi_{i_\eta} - B_w h\phi_i = 0$, while $\hat{\phi}_i$ satisfy $\hat{\phi}_0 - 1 = \hat{\phi}_1 = \hat{\phi}_i = 0$, thus 'homogenizing' the inhomogeneous wall boundary conditions. These new sets of test functions allow the temperature fields in (5.10) to satisfy all their boundary conditions for each problem.

We now let w_j denote the weight functions for the energy equation. In the Galerkin weighted residuals approach, $w_j \equiv \phi_j$. The residuals $\langle w_j, R_T\rangle = 0$, $1 \leqslant j \leqslant m$, for HF can then be written in matrix form as

$$3Pe\left(\boldsymbol{M}_\alpha\ \boldsymbol{A}_t + \boldsymbol{M}_\beta\ \boldsymbol{A}_x + \boldsymbol{M}_\gamma\ \boldsymbol{A} + \boldsymbol{\delta}\right) = \boldsymbol{\Delta} + \boldsymbol{M}_\Gamma\ \boldsymbol{A}, \tag{5.11}$$

where $\boldsymbol{A} = [\theta, A^{(2)}\cdots A^{(m)}]^t$, the matrices $[\boldsymbol{M}_\alpha]_{ij} = \langle\phi_j, \phi_i\rangle$, $[\boldsymbol{M}_\beta]_{ij} = \langle\phi_j, u^{(0)}\phi_i\rangle$, $[\boldsymbol{M}_\gamma]_{ij} = \langle\phi_j, \phi_{it} + u^{(0)}\phi_{ix} + v^{(0)}\phi_{iy}\rangle$ and $[\boldsymbol{M}_\Gamma]_{ij} = \langle\phi_j, \phi_{iyy}\rangle$ are of dimension $m \times m$ and the vectors $[\boldsymbol{\delta}]_j = \langle\phi_j, \phi_{0_t} + u^{(0)}\phi_{0_x} + v^{(0)}\phi_{0_y}\rangle$ and $[\boldsymbol{\Delta}]_j = \langle\phi_j, \phi_{0_{yy}}\rangle$ are of dimension $m \times 1$. The set of equations (5.1*c*), (5.4) and (5.11) will be referred to hereinafter as the GHF[m] model. The corresponding set of equations for ST can be obtained from (5.11) with $\phi_j \to \hat{\phi}_j$. The resulting set of equations will be referred to hereinafter as the GST[m] model.

5.3.2. *Obtaining LWE-HF/LWE-ST from the GHF[m]/GST[m] models*

We now demonstrate that LWE-HF and LWE-ST in §4 can be obtained from an appropriate expansion of GHF and GST. For this purpose we assign the same orders of magnitude for the parameters *Re*, *Pe*, *We*, M, B and B_w as in the LWE. It is important to point out here that our averaged model in (5.11) has been derived without overly restrictive stipulations on the order of the dimensionless groups (see Kalliadasis *et al.* (2003*a*, *b*) for a discussion of lower/upper bounds on the order of

https://doi.org/10.1017/S0022112007008476 Published online by Cambridge University Press

magnitude of the dimensionless parameters). For example, changing the order of Pe in (5.11) would lead to a different long-wave expansion to that obtained in § 4.

Let us now expand q and the amplitudes θ and $A^{(i)}$ as $q = q^0 + \epsilon q^1 + O(\epsilon^2)$, $\theta = \theta_0 + \epsilon^{1-n}\theta_1$, $A^{(i)} = A_{0i} + \epsilon^{1-n} A_{1i}$ where $Pe = O(\epsilon^{-n})$ with $0 < n < 1$ and we truncate our expansions so that terms of $O(\epsilon^2)$ and higher in (5.4) are neglected while terms of $O(\epsilon)$ and higher in (5.11) are neglected. Equation (5.4) then yields

$$q = \tfrac{1}{3}h^3 + \tfrac{2}{5}Re\, h^6 h_x - \tfrac{1}{3}h^3 h_x \cot\beta - \tfrac{1}{2}Mh^2\theta_x + \tfrac{1}{3}Weh^3 h_{xxx}. \tag{5.12}$$

We note that at this point θ_x from the averaged system in (5.11) remains undetermined, however, we shall demonstrate that it is identical to that obtained from LWE.

Substituting q from (5.12) into (5.11), the ϵ^{1-n}-expansions for the temperature and using the kinematic boundary condition (5.1c) yields:

$$\theta = F + \tfrac{1}{40}PeBGh^3 h_x, \quad A^{(2)} = \tfrac{1}{2}PeB^2(1 - B_w h)F^2 h^4 h_x,$$
$$A^{(3)} = \tfrac{1}{8}PeB_w B(1 + 3Bh)F^2 h^4 h_x, \quad A^{(4)} = -\tfrac{3}{40}PeB_w B^2 F^2 h^5 h_x.$$

We also have $A^{(i)} = 0$ for $i \geqslant 5$, for HF, while for ST we have

$$\theta = \hat{F} + \tfrac{1}{40}Pe\hat{B}\hat{G}h^3 h_x, \quad A^{(2)} = \tfrac{1}{8}Pe\hat{B}(1 + 3\hat{B}h)\hat{F}^2 h^4 h_x, \quad A^{(3)} = -\tfrac{3}{40}Pe\hat{B}^2\hat{F}^2 h^5 h_x,$$

with $A^{(i)} = 0$ for $i \geqslant 4$. The expressions for θ are then substituted into (5.12), which in turn is substituted into the kinematic condition (5.1c) to yield LWE-HF given in (4.1) and the corresponding equation for LWE-ST. Further, when all the amplitude functions are substituted into (5.10a) and (5.10b), we obtain exactly the same temperature fields as those given in (A 1a) and (A 1b).

Hence, we have demonstrated that in order to obtain the long-wave theory of § 4 to $O(\epsilon Pe)$ from an appropriate expansion of our Galerkin system, and hence fully resolve the behaviour close to criticality, we require that $m \geqslant 4$ for HF and $m \geqslant 3$ for ST.

Finally, we note that in the limit $\bar{h}_N \to 0$ (so that $Re, Pe \to 0$) all models including SST and SHF reduce to the corresponding LWE models in this limit. This expansion should not be confused with the ϵ-gradient expansion for fixed $\bar{h}_N$ performed above for the GHF/GST models to fully recover the LWE model.

5.3.3. *Single-mode Galerkin residuals approach: the GHF[1] and GST[1] models*

Although 4 and 3 are the minimum dimensionalities to fully resolve the behaviour of long waves for HF and ST, respectively, for convenience we shall investigate the models obtained at the lowest possible level of truncation, i.e. for $m = 1$. At this level, the temperature profiles for HF and ST are quadratic and cubic in η, respectively, $T = \phi_0 + \theta\phi_1$ and $T = \hat{\phi}_0 + \theta\hat{\phi}_1$. The relative simplicity, at least compared to the higher-order projections, of the $m = 1$ models makes them useful prototypes for numerical and mathematical scrutiny. Appendix B gives explicitly (5.11) for $m = 1$. The linear stability analysis of these models is done similarly to that of the SHF/SST models in § 5.2.2. Table 1 summarizes the different models.

6. Comparisons

In all our computations we take $\beta = \pi/2$, $Ka = 3000$ and $Pr = 7$; however, in order to assess the influence of the convective heat transport effects we shall sometimes include results with $Pr = 1$. Also as stated in § 4.3, we take $\hat{Bi} = 0.1$ along with the two parameter sets defined for Bi_w, Bi and Ma. Recall that these sets of values have

https://doi.org/10.1017/S0022112007008476 Published online by Cambridge University Press

LWE-HF	LWE-ST	SHF	SST	GHF[1]	GST[1]
		(5.1*c*)	(5.1*c*)	(5.1*c*)	(5.1*c*)
(4.1*a*)	(4.1*b*)	(5.4)	(5.4)	(5.4)	(5.4)
		(5.8*a*)	(5.8*b*)	(B 1*a*)	(B 1*b*)

TABLE 1. Summary of equations for the different time-dependent models: LWE – long-wave expansion (§ 4.1), SHF/SST – simple heat flux/specified temperature (§ 5.2.1), GHF[1]/GST[1] – single-model Galerkin approach for heat flux/specified temperature (§ 5.3.1, Appendix B). The corresponding travelling-wave models are obtained by introducing into the time-dependent models the moving coordinate $Z = X - c\Theta$ with $\partial/\partial\Theta = -c\partial/\partial Z$.

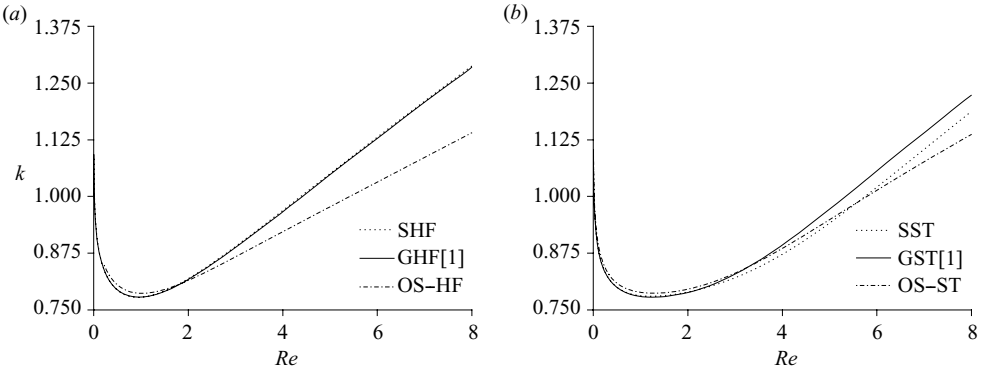


FIGURE 2. Neutral stability curves in the wavenumber $k - Re$ plane with $Pr = 7$; (*a*) HF for $Ma = 21.6$, $Bi_w = 0.6$, $Bi = 0.12$; (*b*) ST for $\hat{M}a = 30$ and $\hat{B}i = 0.1$.

been chosen in order to allow the HF and ST problems to have the same long-wave limits as Re tends to zero.

6.1. *Neutral stability curves*

Figure 2 illustrates typical curves for the neutral wavenumber of infinitesimal disturbances as a function of Re obtained from the averaged models and the Orr–Sommerfeld analysis for the HF and ST cases, referred to as OS-HF and OS-ST, respectively. For consistency with the other models, the Orr–Sommerfeld wavenumber has been scaled with $1/We^{1/3}$.

For small Re, all models agree. In fact, as Re tends to zero, the neutral wavenumber tends to infinity for both ST and HF cases. For the ST case, this is in agreement with the OS-ST analysis by Scheid *et al.* (2005). This behaviour is also consistent with our analysis in § 5.2.2 of the neutral curve of the SHF and SST models in the limit of small film thicknesses. This behaviour indicates that the Marangoni effect is stronger in this region. We shall return to this point when we discuss the nonlinear regime. As Re now increases, our models predict slightly smaller wavenumbers than OS-HF/ST initially, but further increasing Re shows that our models overpredict the neutral wavenumbers and they increasingly deviate from OS-HF/ST. This is to be expected as we have not taken into account the second-order dissipative effects. As was shown by Scheid *et al.* (2005) for the ST case, taking these terms into account leads to a good agreement of the resulting Galerkin model with OS-ST for a much larger region of Reynolds numbers. Finally, we note that for the HF case, our models are almost graphically indistinguishable from each other over the entire range of

https://doi.org/10.1017/S0022112007008476 Published online by Cambridge University Press

Reynolds numbers in figure 2(*a*) and they both start to diverge from OS-HF at $Re \sim 2$. For the ST case, both models follow a similar path; however, the SST model performs better than the GST[1] with the divergence of SST at around $Re \sim 6$.

6.2. *Solitary waves*

We now seek travelling-wave solutions propagating at a constant speed c. We introduce the moving coordinate transformation $Z = X - c\Theta$ in the time-dependent models of table 1 with $\partial/\partial\Theta = -c\partial/\partial Z$ for the waves to be stationary in the moving frame.

The equation obtained from the LWE model in (4.2) in the moving frame can then be integrated once with the integration constant determined from the far-field condition $h \to 1$ as $Z \to \pm\infty$ which leads to a nonlinear eigenvalue problem for the speed of the travelling waves c. For the weighted residuals models we use the kinematic condition (5.1*c*) which in the moving frame yields $-ch' + q' = 0$. This can be integrated once and we fix the integration constant by demanding $h, q \to 1, 1/3$ as $Z \to \pm\infty$. This gives a relation between the flow rate and the film thickness, $q = (1/3) + c(h - 1)$. The SHF/GHF[1] travelling-wave models consist of (5.4) and (5.8*a*)/(B 1*a*) in the moving frame and with q eliminated from the above expression. These equations along with the boundary conditions $h(\pm\infty) = 1$ and $\theta(\pm\infty) = \overline{F}$ define the SHF/GHF[1] nonlinear eigenvalue problems for the speed c of the solitary waves. Finally, the SST/GST[1] travelling-wave models consist of (5.4) and (5.8*b*)/(B 1*b*) in the moving frame and with q eliminated from the above expression. These equations, along with the boundary conditions $h(\pm\infty) = 1$ and $\theta(\pm\infty) = \hat{\overline{F}}$, define the SHF/GHF[1] nonlinear eigenvalue problems for the speed c of the solitary waves.

Here we restrict our attention to single-hump solitary waves. They correspond to the principal homoclinic orbits of the dynamical systems corresponding to the travelling-wave models. We compute them using the continuation software AUTO97 (Doedel *et al.* 1997). Appendix C analyses the linearized travelling-wave equations for the different models and provides necessary conditions for the existence of solitary waves and sufficient conditions for the non-existence of such waves.

Figure 3 shows typical bifurcation diagrams for the speed c of the solitary waves as a function of Re. Figures 3(*a*)–3(*c*) depict bifurcation diagrams for positive-hump waves (characterized by $c > 1$) and figure 3(*d*) negative-hump waves (characterized by $c < 1$). The ST problem has positive-hump waves only while the HF problem has negative-hump waves co-existing with positive-hump ones. The ST problem admits negative multi-hump waves, but, as we pointed out earlier, here we focus on single-hump waves only.

We first discuss figure 3(*a–c*). Following our discussion in § 4.3, we take in these figures two sets of parameter values with $Bi_w = Bi = 0.2$ and $Bi_w = 0.6$, $Bi = 0.12$ (our discussion in § 4.3 was based on LWE, but for comparison purposes we choose the same values for the other models). For the ST models we take $\hat{M}a = 0$, 30 and 75. Hence, the first set of values for the HF models is $Ma = 0$, 12 and 30 and the second set is $Ma = 0$, 21.6 and 54.

As Re tends to zero, the speed (and amplitude) of the solitary pulses tends to infinity. This is consistent with the linear stability analysis in figure 2 which indicates that the influence of the Marangoni effect is larger for small Re. This unusual behaviour was first pointed out for the ST case by Kalliadasis *et al.* (2003*b*) and was further discussed by Scheid *et al.* (2005). In the limit of vanishing Reynolds number, inertia effects are negligible and the Marangoni effect is very strong. This is also evident from our scalings in § 2.2, $M = Ma/\bar{h}_N$ and $\hat{M} = \hat{M}a/\bar{h}_N^2$, which show that $M, \hat{M} \to \infty$ as

https://doi.org/10.1017/S0022112007008476 Published online by Cambridge University Press

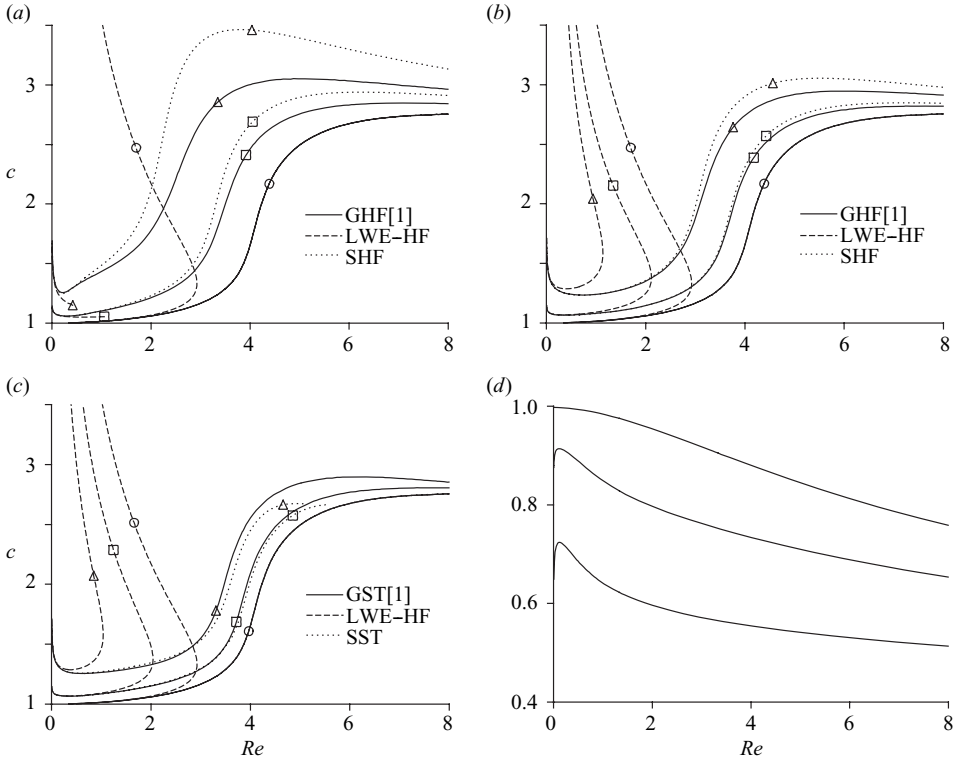


FIGURE 3. Single-hump solitary-wave bifurcation diagrams for the speed c as a function of Reynolds number Re from various models with $Pr = 7$. The circles in (a–c) correspond to $Ma = \hat{M}a = 0$. (a–c) represent positive-hump waves and (d) negative-hump ones; (a) HF with $Bi_w = Bi = 0.2$; the square corresponds to $Ma = 12$ and the triangle to $Ma = 30$; (b) HF with $Bi_w = 0.6$ and $Bi = 0.12$; the square corresponds to $Ma = 21.6$ and the triangle to $Ma = 54$; (c) ST with $\hat{B}i = 0.1$; the square corresponds to $\hat{M}a = 30$ and the triangle to $\hat{M}a = 75$; (d) GHF[1] with $Bi_w = 0.12$ and $Bi = 0.6$. The three lines correspond to $Ma = 0$, $Ma = 21.6$ and $Ma = 54$, from top to bottom, respectively.

$\bar{h}_N \to 0$. In this region of small film thicknesses, the destabilizing forces are interfacial forces owing to the Marangoni effect (capillary forces are always stabilizing). Contrast with the isothermal falling film where the only destabilizing forces are inertia forces which are vanishing as Re tends to zero so that c in this region should approach the infinitesimal wave speed 1, as the $Ma = \hat{M}a = 0$ curves in figure 3 do. In the presence of the Marangoni effect, our computations indicate that for $Re \to 0$ the width of the solitary pulses also tends to infinity, but at a rate faster than that for the amplitude, so that the long-wave approximation is not violated. However, as was emphasized by Kalliadasis *et al.* (2003*b*) this behaviour for $Re \to 0$ does not correspond to a true singularity formation as other forces of non-hydrodynamic origin (e.g. long-range attractive intermolecular interactions) which have not been included here become predominant in this region, thus arresting the singularity formation (in other words the zero-Re limit is never reached).

On the other hand, for large film thicknesses, inertia forces dominate Marangoni forces and in fact $M, \hat{M} \to 0$ as $\bar{h}_N \to \infty$ so that the Marangoni forces diminish in this limit and the temperature field has only a weak effect on the hydrodynamics. Hence, for large Re, the different $M, \hat{M}$ curves should merge into a single curve, as

https://doi.org/10.1017/S0022112007008476 Published online by Cambridge University Press

figures 3(*a*) to 3(*c*) indicate. This curve seems to asymptote towards a certain value for large Re which is the same to that in the isothermal case. Here we do not track the solution branches beyond $Re = 8$. In any event, in the region of relatively large Re, one-dimensional solitary pulses could develop instabilities in the transverse direction.

Figures 3(*a*) to 3(*c*) indicate that both LWE models exhibit an unrealistic behaviour with branch multiplicity and turning points at particular values of Re. By analogy now with the isothermal case, and as we discussed in § 1, we expect that LWE exhibits a finite-time blow-up behaviour for Re larger than the values corresponding to the turning points (this has been confirmed by time-dependent computations). Obviously, this catastrophic behaviour is related to the non-existence of solitary waves and indicates the inability of LWE to describe nonlinear waves correctly far from criticality. Moreover figure 3(*a*) shows the existence of limit points where LWE simply terminates, not observed before in studies of the isothermal falling film. In Appendix C1, we show that this corresponds to all of the spatial eigenvalues of the linearized system at $h = 1$ having real parts with the same sign so that homoclinic orbits do not exist.

Figures 3(*a*) to 3(*c*) also indicate that all models collapse into a single line in the region $Re \to 0$. This is consistent with our observation at the end of § 5.3.2. Also for $Ma = \hat{M}a = 0$ (curves marked with a circle) the figures 3(*a*) to 3(*c*) give the same solution branches for each of the LWE, simple weighted residuals and Galerkin approximations, as expected. We note that figures 3(*b*) and 3(*c*) (with the exception of the $Ma = \hat{M}a = 0$ curves) are almost identical for LWE. This is consistent with our discussion in § 4.3: indeed $\mathscr{C} > 0$ in figure 3(*b*) whereas for LWE-ST $\hat{\mathscr{C}}$ is always > 0. The Galerkin models in figures 3(*b*) and 3(*c*) are qualitatively similar, note, however, the relatively flat region around $Re \sim 2$ for GST[1] with $\hat{M}a = 75$. The simple weighted residuals models in figures 3(*b*) and 3(*c*) are also qualitatively similar, notice however, that SHF is slightly above GHF[1] in figure 3(*b*) and slightly below GHF[1] in figure 3(*c*). Note that in figure 3(*c*), we were not able to continue the numerical solution to Re above ~ 5 because the coefficient of θ_Z is close to zero in this region (see § 8.3). This is purely a numerical difficulty and does not imply that the solution ceases to exist after this point.

Further, we note that figures 3(*a*) and 3(*b*) (again with the exception of the $Ma = \hat{M}a = 0$ curves) are different for all LWE models. Now $\mathscr{C} < 0$ in figure 3(*a*), whereas for LWE-ST, $\hat{\mathscr{C}}$ is always > 0. Following then from our discussion in § 4.3, the LWE-HF and LWE-ST models show different behaviours. The simple weighted residuals and Galerkin models in figures 3(*a*) are qualitatively similar to those in figure 3(*b*), however, a marked difference between the two is observed as the Marangoni number increases. Note also that in figure 3(*a*), the SHF model predicts faster waves than the GHF[1] model whereas in figure 3(*c*) we see that the SST model predicts slower waves than the GST[1] model.

We now turn to the negative-hump waves in figure 3(*d*). With the exception of the $Ma = 0$ curve that approaches the speed of 1 as Re tends to zero, for the remaining curves, the speed approaches minus infinity, consistent with our earlier observation that the Marangoni effect is very strong in this region. Again, forces of non-hydrodynamic origin such as intermolecular interactions would introduce a lower bound here, especially as for negative-hump waves the largest free-surface deformation is towards the wall. On the other hand, for large Re, all curves merge into a single one as with the positive-hump waves, but we must go to sufficiently large Re, e.g. for $Re > 60$ the three different curves have speeds in the interval $[0.4, 0.5]$. The final asymptotic value for the three curves is $c \sim 0.4$.

https://doi.org/10.1017/S0022112007008476 Published online by Cambridge University Press

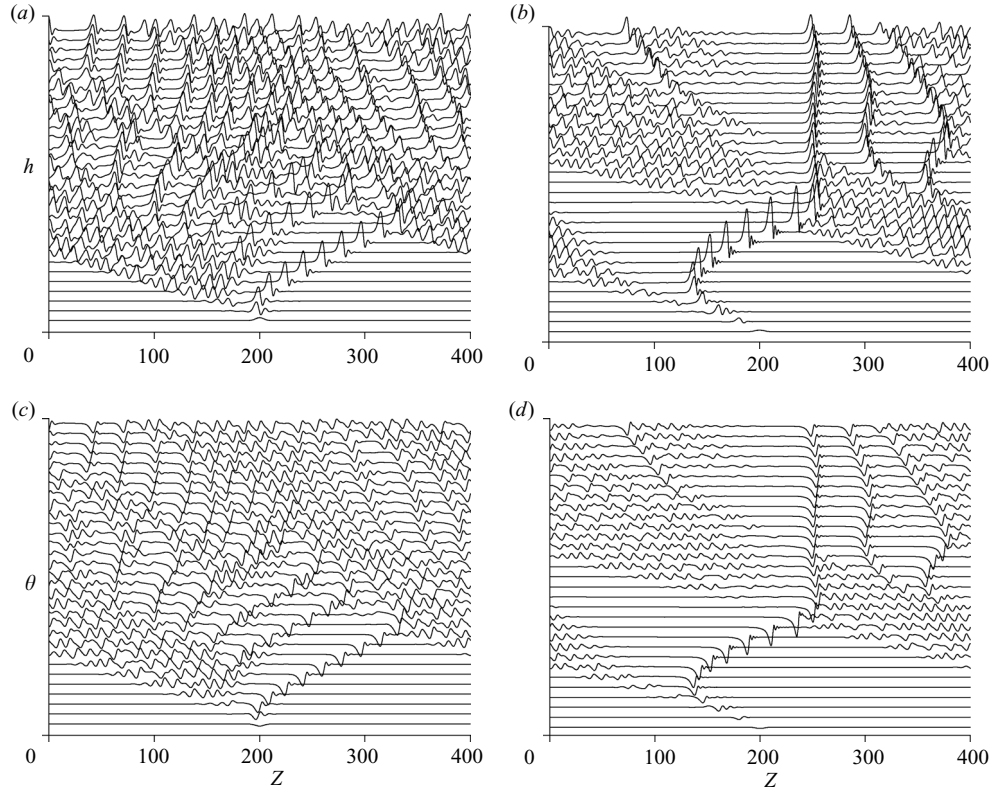


FIGURE 4. Time evolution for the free surface (a, b) and interfacial temperature (c, d) in an extended domain for GST[1] and in a coordinate system moving with speed c. $\hat{Bi} = 0.1$, $\hat{Ma} = 30$ and $Pr = 7$. In (a, c) $c = 1.1$ for $Re = 3$ and in (b, d) $c = 1.46$ for $Re = 4$. Successive curves in (a, c) are separated by $\Delta\Theta = 100$ with $\Theta \in [0, 3 \times 10^3]$ and in (b, d) by $\Delta\Theta = 50$ with $\Theta \in [0, 1.5 \times 10^3]$.

7. Spatio-temporal dynamics

We now illustrate the spatio-temporal dynamics of the heated falling film by using the GST[1] and GHF[1] models. The previous studies by Kalliadasis *et al.* (2003*b*) and Scheid *et al.* (2005) on heated falling films focused on the construction of stationary solitary waves only (using ST) without any time-dependent computations. For our computations we employ a Crank–Nicolson-type implicit scheme with the spatial derivatives approximated by central differences and with dynamic time-step adjustment. We impose periodic boundary conditions over a domain much larger than the maximum growing wavelength predicted by linear stability. The initial condition is a Gaussian distribution in the middle of the domain. The computations are performed in the moving frame $Z = (x - ct)/We^{1/3}$ with time given by $\Theta = t/We^{1/3}$.

Typical time evolutions of the free surface and interfacial temperature for the GST[1] model are shown in figure 4 for $\hat{Bi} = 0.1$, $\hat{Ma} = 30$ and $Pr = 7$, corresponding to the parameter values in figure 3(*c*) with $\hat{Ma} = 30$. Within the inception region, the wave amplitude grows exponentially in time, as predicted by linear stability. Immediately beyond it, the waves begin to steepen in front and develop a back shoulder, signifying a weakly nonlinear excitation of an overtone. The amplitude modulation still persists; however, the larger waves now begin to accelerate, they

https://doi.org/10.1017/S0022112007008476 Published online by Cambridge University Press

collide with the smaller waves in front of them and eventually overtake them. These coalescence events are evident for both free surface and interfacial temperature.

For $Re = 3$, figure 4(a) shows that the final result of the evolution is a train of soliton-like coherent structures with almost the same amplitude and which interact indefinitely with each other like in soliton–soliton elastic collision. For $Re = 4$, figure 4(b) shows that the final result of the evolution is three large-amplitude waves, each of which preceded by a train of small-amplitude soliton-like coherent structures. The large waves collide with the smaller waves at the front and eventually absorb them, leaving a flat region behind them. Because of the flat-film instability, waves begin to grow in the flat-film region behind the large waves and they start to evolve towards solitary wavetrains. However, owing to the periodicity, they cannot escape from the large-amplitude waves which collide with these smaller waves and overtake them.

These coherent structures possess a gentle sloped back edge and a steep front edge preceded by some small bow waves and are reminiscent of the infinite-domain positive-hump solitary pulses obtained in § 6.2 (figure 3c with $\hat{M}a = 30$). However, the wavespeeds predicted by the time-dependent calculations are smaller than those predicted by the stationary travelling-wave calculations. This is due to the time-dependent calculations having an average film thickness of 1, whereas the stationary travelling waves approach a flat-film region close to 1 far from their hump so that their average film thickness is greater than 1. As the film thickness is smaller and the wave speed has been scaled with the film thickness, we expect that the resulting wave speed in time-dependent computations will also be smaller.

In all cases, the interfacial temperature is similar to an inverse of the free surface. Further, we note that for the Re values in figure 4, LWE does not have any solitary wave solutions (see figure 3c with $\hat{M}a = 30$). In fact, time-dependent computations of LWE show that it blows up in finite time for the parameter values in figure 4. Unlike LWE, our models are quite robust and they do not exhibit any singularity formation.

Figure 5 depicts a typical time evolution obtained from the GHF[1] model for $Pr = 7$, $Re = 3$ and the two sets of values, $[Bi_w, Bi, Ma] = [0.2, 0.2, 12]$ and $[Bi_w, Bi, Ma] = [0.6, 0.12, 21.6]$, corresponding to the travelling-wave bifurcation diagrams in figure 3(a) with $Ma = 12$ and figure 3(b) with $Ma = 21.6$, respectively. Again, the free surface approaches a train of coherent structures that resemble the infinite-domain positive-hump waves computed in figures 3(a) and 3(b) whereas the interfacial temperature is similar to an inverse of the free surface.

Additional computations with the GHF[1] model are shown in figure 6. In figure 6(a, c), $Re = 1$, $Pr = 7$ and $[Bi_w, Bi, Ma] = [0.12, 0.6, 21.6]$, corresponding to the middle curve of the travelling-wave bifurcation diagram in figure 3(d). The initial condition starts to grow into an expanding radiation wavepacket. Positive-hump waves are created from the front of the wavepacket and negative-hump ones from its back. These negative-hump waves correspond to those computed in figure 3(d). The system eventually approaches a train of coherent structures consisting of co-existing positive- and negative-hump waves. Stationary travelling negative-hump waves also exist in isothermal films, but they are unstable in time-dependent computations (Chang & Demekhin 2002). Increasing the Reynolds number to $Re = 3$ in figures 6(b) and 6(d) suppresses the negative-hump waves and leads to a train of positive-hump ones. Note that the large-time behaviour of the free surface in figure 6(a) is reminiscent of the Kuramoto–Sivashinsky (KS) spatio-temporal chaos/turbulent-like dynamics. On the other hand, in figure 6(b), the surface approaches a series of 'bound states' like in Kawahara equation (KS with dispersion) for sufficiently large dispersion (Kawahara 1983). This highlights the significance of the dispersive effect associated with the

https://doi.org/10.1017/S0022112007008476 Published online by Cambridge University Press

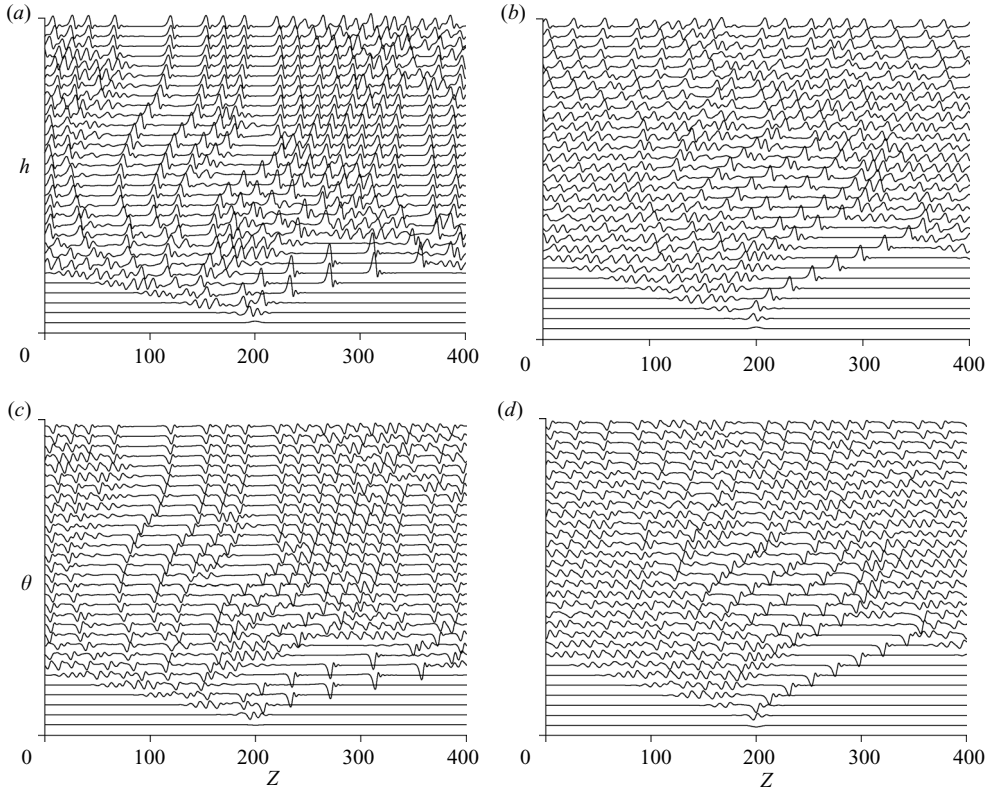


FIGURE 5. Time evolution for the free surface (a, b) and interfacial temperature (c, d) in an extended domain for GHF[1] and in a coordinate system moving with speed c. $Pr = 7$ and $Re = 3$ in a coordinate system moving with a speed c. In (a, c) $c = 1.135$ for $Bi = Bi_w = 0.2$ and $Ma = 12$ and in (b, d) $c = 1.1$ for $Bi = 0.12$, $Bi_w = 0.6$ and $Ma = 21.6$. Successive curves are separated by $\Delta\Theta = 100$ with $\Theta \in [0, 3 \times 10^3]$.

Péclet number: increasing the Péclet number 'regularizes' the system and selects a regular train of large-amplitude solitary pulses.

8. Finite-difference solutions of the energy equation for HF and ST: FDHF and FDST

We now contrast the interfacial temperature distribution obtained from our (one-dimensional) one-mode averaged models with the solution of the two-dimensional energy equation in (5.7), which is after all the equation we are trying to model. We set $Ma = \hat{M}a = 0$. The reason for this is two-fold. (i) The hydrodynamic and thermal problems are decoupled so that the temperature field does not have any influence on the film thickness. However, the evolution of the film thickness does affect the temperature field. We emphasize that Shkadov's IBL solitary-wave-solution branches are in quantitative agreement with the boundary-layer (Demekhin, Kaplan & Shkadov 1987) and full Navier–Stokes equations (Salamon, Armstrong & Brown 1994; Ramaswamy, Chippada & Joo 1996) while the single-mode corrected Shkadov model in (5.4) (with $M = 0$) is in quantitative agreement with full Navier–Stokes (Ruyer-Quil & Manneville 2000, 2002). Hence we do have a proper description of

https://doi.org/10.1017/S0022112007008476 Published online by Cambridge University Press

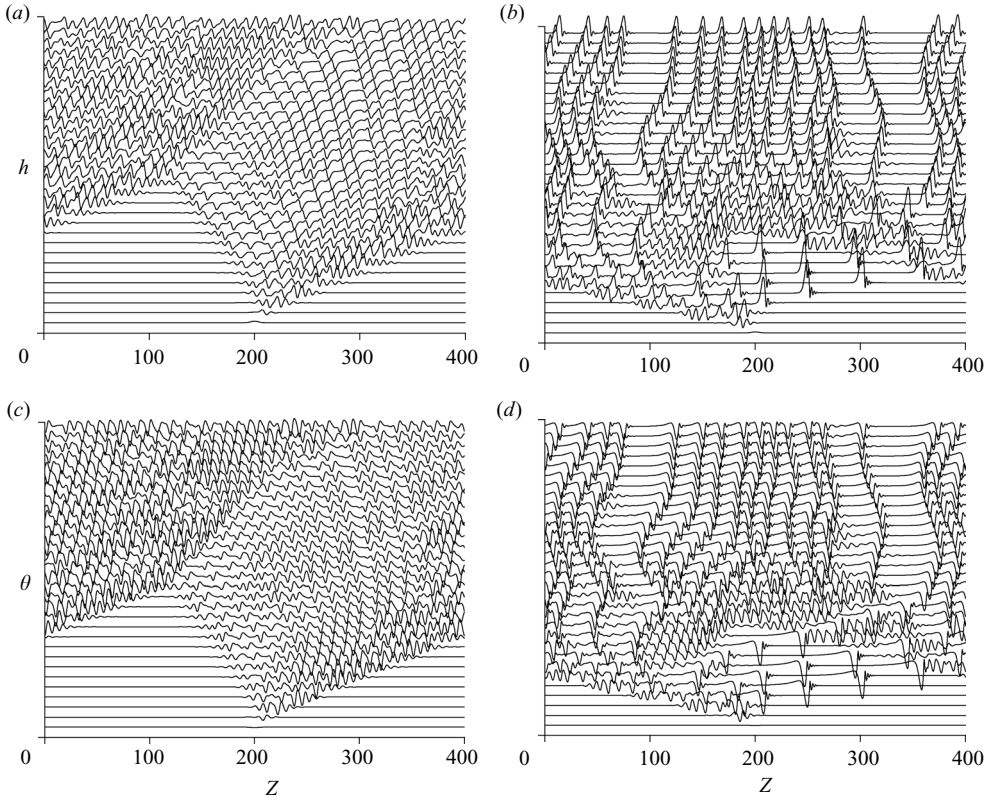


FIGURE 6. Time evolution for the free surface (a, b) and interfacial temperature (c, d) in an extended domain for GHF[1] and in a coordinate system moving with a speed c. $Pr = 7$, $Bi_w = 0.12$, $Bi = 0.6$ and $Ma = 21.6$. In (a, c) $c = 1.0$ for $Re = 1$ and in (b, d) $c = 1.4$ for $Re = 3$. Successive curves are separated by $\Delta\Theta = 50$ with $\Theta \in [0, 1.5 \times 10^3]$.

the hydrodynamics. (ii) The decoupling of hydrodynamics from energy significantly simplifies the computations of the two-dimensional temperature field.

Substituting the flow field from (5.2) and (2.5a) into (5.7), we obtain

$$T_{\eta\eta} = \frac{Pr\delta}{2}[(3qh(2\eta - \eta^2) - 2ch^2)T_Z + chh_Z\eta(\eta - 1)(\eta - 2)T_\eta], \tag{8.1a}$$

subject to the boundary conditions

$$T_\eta = -BhT \quad \text{on} \quad \eta = 1, \tag{8.1b}$$

$$T_\eta = -h + B_w hT \quad \text{on} \quad \eta = 0 \text{ for HF}, \tag{8.1c}$$

$$T = 1 \quad \text{on} \quad \eta = 0 \text{ for ST}, \tag{8.1d}$$

which is solved in two dimensions along with periodic boundary conditions in the Z-direction where h is obtained from the isothermal momentum equation (5.4) in the moving frame Z with $q = 1/3 + c(h - 1)$. The above system was solved numerically using a finite-differencing scheme. We shall refer to the numerical solution of (8.1a), (8.1b) and (8.1c) as 'finite differences for HF' or FDHF and the numerical solution of (8.1a), (8.1b) and (8.1d) as 'finite differences for ST' or FDST. Note that although the computations were performed over an extended domain here we only illustrate the solutions near the wave maximum.

https://doi.org/10.1017/S0022112007008476 Published online by Cambridge University Press

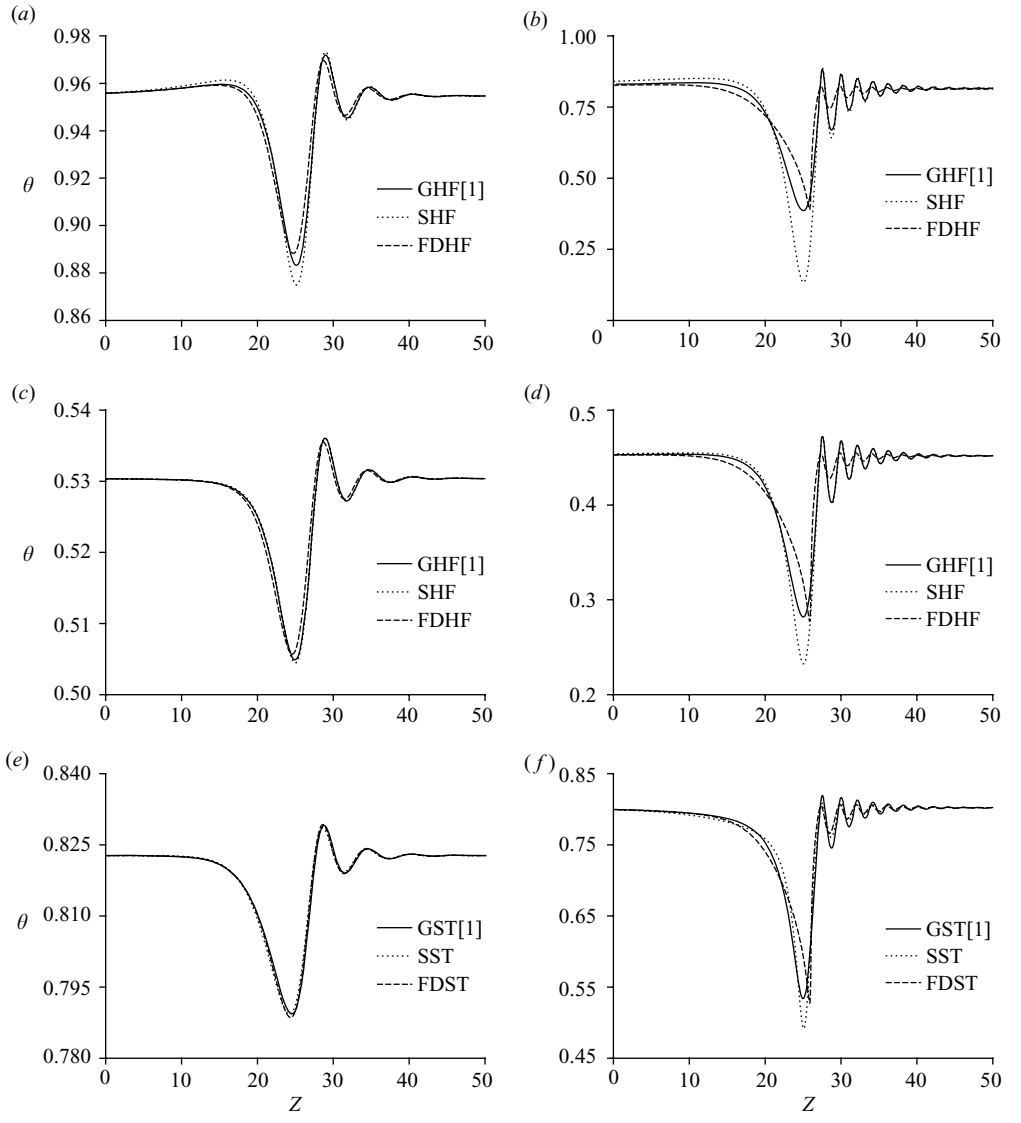


FIGURE 7. Comparison of the interfacial temperature distribution obtained from various models for $Ma = \hat{M}a = 0$ and $Pr = 7$. In (a, b) (HF) for $Bi_w = Bi = 0.2$. In (c, d) HF for $Bi_w = 0.6$ and $Bi = 0.12$. In (e, f) ST for $\hat{B}i = 0.1$. In (a, c, e) $Re = 10/3$ and in (b, d, f) $Re = 5$.

Figure 7 compares the temperature distributions obtained for the different models for $Pr = 7$, $Ma = \hat{M}a = 0$ and in the region of moderate Re. LWE is not included as in this region it does not predict the existence of solitary waves. All models use the same isothermal fluid flow and free surface. Clearly, for small values of Re, all models are in good agreement, as expected. For larger Re, we observe a difference between our models and FD. This difference increases as Re increases. More specifically, figures 7(a), 7(c) and 7(e) for $Re = 10/3$ show that the interfacial temperature distributions obtained from our averaged models for both HF and ST are quite close to FDHF and FDST, respectively. Figures 7(b), 7(d) and 7(f) for $Re = 5$ show that the Galerkin models for both HF and ST predict a similar interfacial temperature minimum to that

https://doi.org/10.1017/S0022112007008476 Published online by Cambridge University Press

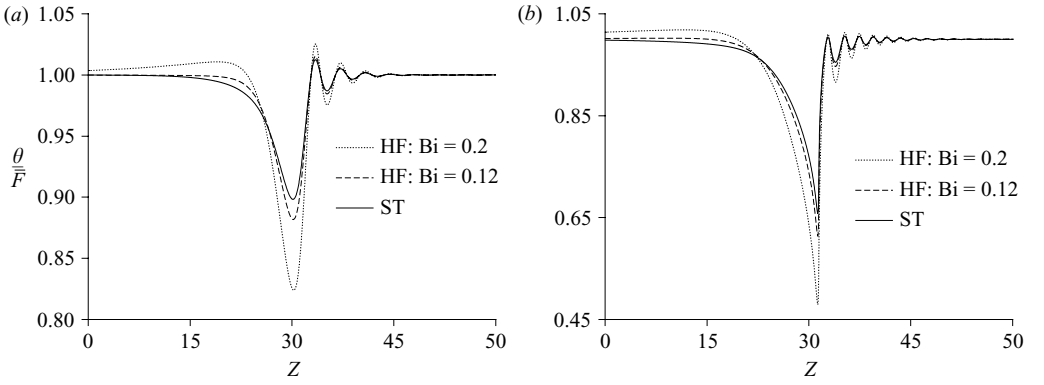


FIGURE 8. Normalized interfacial temperature for FDHF and FDST with $Ma = \hat{M}a = 0$ and $Pr = 7$. In (*a*) $Re = 3$ and in (*b*) $Re = 4$. $Bi_w = 0.2$ when $Bi = 0.2$ and $Bi_w = 0.6$ when $Bi = 0.12$.

obtained from FDHF and FDST. The simplified models on the other hand follow closely the front of the interfacial temperature wave, but they overshoot the minimum.

Let us now compare HF and ST with each other. For this purpose we plot the normalized interfacial temperature distributions $\theta/\overline{F}$ for HF and $\theta/\hat{F}$ for ST so that both normalized profiles lead to a flat-film solution of unity. Figure 8 depicts the normalized FDHF and FDST solutions for $Re = 3$ and $Re = 4$. At the front of the interfacial temperature wave, both rescaled temperatures are very similar. There is, however, a marked difference for the temperature minimum, with the FDHF solution for $Bi = Bi_w = 0.2$ predicting the lowest minimum, and the FDST solution predicting the highest minimum. The FDHF model with $Bi = 0.12$ and $Bi_w = 0.6$ follows the FDST solution quite closely. The FDHF solution for $Bi = Bi_w = 0.2$, also predicts the longest tail for the rescaled interfacial temperature at the back of the wave. Further, an overshoot at the back of the wave is present for the FDHF solution for $Bi = Bi_w = 0.2$, unlike the other two solutions.

FDHF for the second set of values, namely $Bi = 0.12$ and $Bi_w = 0.6$ which satisfies $Bi_w > Bi$ (see § 4) produces results fairly close to those obtained from FDST. Hence, for convenience we shall illustrate only results for the ST problem in the remainder of this study.

8.1. *Recirculation zones*

With reference now to figure 7, we have found that all our averaged models are in good agreement with FD, provided that $Re \lesssim 4.5$. For larger values of Re, a slender clockwise-turning recirculation zone appears inside the solitary wave. This zone is accompanied by two stagnation points, one at the front and one at the back of the wave (recall that the computations are done in the moving frame).

8.1.1. *On the validity of the long-wave approach in the presence of recirculation zones*

The presence of recirculation zones does not invalidate the assumption $u \gg v$ necessary for the long-wave approximation. The computed streamlines correspond to envelopes of the velocity field in the moving frame $(U, v)^t$ with $U = u - c$. Recirculation zones indicate regions where $v \gg U$, e.g. points where the flow returns with $U = 0$ and the stagnation points where $U = v = 0$. However, in the laboratory frame, these regions have $u = c \gg v$ so that the conditions $u \gg v$ in the laboratory frame and $v \gg U$ in the moving frame can both hold at the same time.

https://doi.org/10.1017/S0022112007008476 Published online by Cambridge University Press

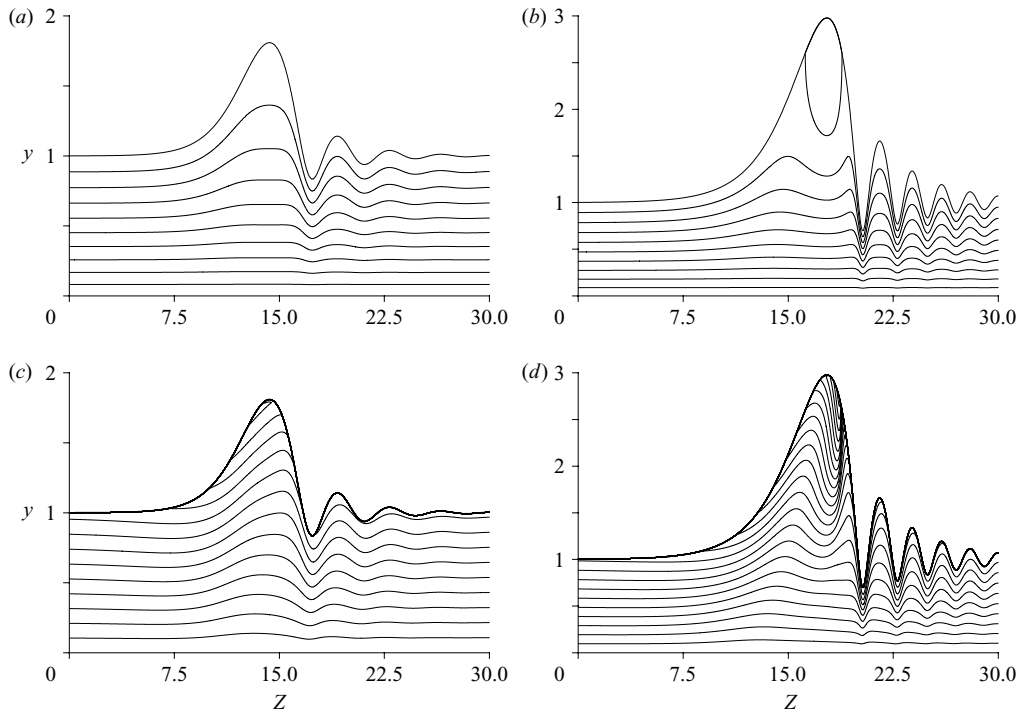


FIGURE 9. Streamlines (a, b) and isotherms (c, d) obtained computationally from FDST with $\hat{M}a = 0$, $\hat{B}i = 0.1$ and $Pr = 7$. In (a, c) $Re = 4$ and in (b, d) $Re = 5$.

It is important to emphasize that if closed streamlines exist in the moving frame, a fluid particle is trapped in both moving and laboratory frames. Hence, solitary waves with recirculation zones 'transport' the trapped fluid mass downstream (in fact this is the chief mechanism behind heat/mass transport enhancement in wavy interfaces). However, the streamlines in the laboratory frame are not closed; in this frame, a particle simply moves faster and slower to the wave crest at the top and bottom halves of the (moving frame) recirculation zone, respectively.

Hence the appearance of the recirculation zone is a manifestation of the moving frame. Clearly, in the laboratory frame all of the fluid will move forward without any recirculation. It is precisely for this reason that the long-wave assumption still holds. In fact, as emphasized earlier, for isothermal films, the Shkadov IBL solitary waves are in good agreement with direct numerical simulations of full Navier–Stokes (the same is true for the solitary waves of a model obtained by a high-order weighted residual technique (Ruyer-Quil & Manneville 2002)) despite the fact that for the solitary waves of largest amplitude a recirculation zone is present below the hump. Similarly, the long-wave approximation has been successful in describing recirculation zones in different settings, including the problem of a moving contact line where a recirculation zone can occur below the capillary ridge appearing in the immediate vicinity of the contact line (Goodwin & Homsy 1991).

8.2. *Thermal boundary layers*

In figure 9, we show streamlines and isotherms in the absence of the Marangoni effect with $Pr = 7$ and $Re = 4, 5$ obtained from FDST. As is evident from figure 9(c, d), the presence of the recirculation zone dramatically alters the topology of the isotherms.

https://doi.org/10.1017/S0022112007008476 Published online by Cambridge University Press

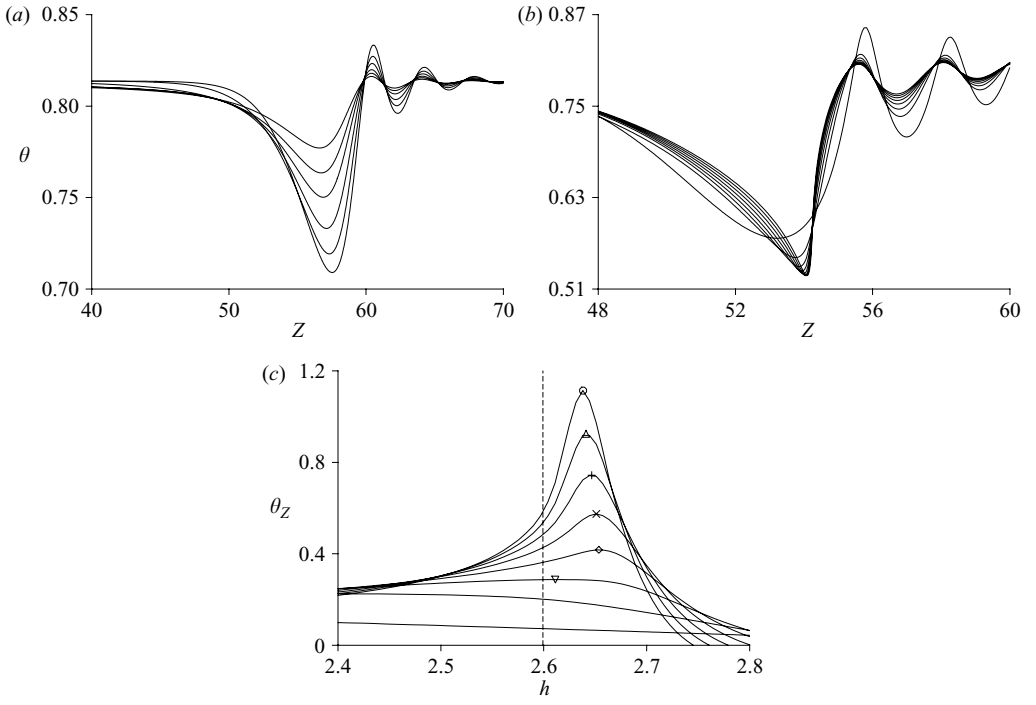


FIGURE 10. The interfacial temperature against Z and the gradient of the interfacial temperature against h, obtained computationally from FDST with $\hat{M}a = 0$ and $\hat{B}i = 0.1$. In (*a*) $Re = 4$ and $Pr = 1, 3, 8, 20, 40$ and 90 and in (*b*, *c*) $Re = 5$ and $Pr = 0$ to 7 in increments of 1. The vertical dashed line in (*c*) denotes the location of the stagnation point.

For $Re = 4$, the isotherms are nearly aligned whereas for $Re = 5$, they are deflected upwards owing to the movement of the fluid in the recirculation zone. This tightening of the isotherms occurs in the vicinity of the front stagnation point in the flow associated with the formation of steep temperature gradients there. The formation of steep temperature gradients close to the front stagnation point was also shown by Scheid *et al.* (2005) by using the weighted residuals models developed by Ruyer-Quil *et al.* (2005)(systems (4.18) and (6.6) in their study).

In figure 10, we illustrate the effect of the Péclet number on the heat transport process before and after the recirculation zone appears. The interfacial temperature distribution is obtained from FDST. In figure 10(*a*), we take $Re = 4$ in which case a recirculation zone does not exist, whereas in figure 10(*b*), we take $Re = 5$ in which case a recirculation zone is present. In the absence of a recirculation zone, increasing the Péclet number dampens the free-surface temperature distribution. On the other hand, when a recirculation zone is present, increasing the Péclet number causes a sharp gradient on the free-surface temperature distribution. Figure 10(*c*) shows that the sharp gradient appears in the vicinity of the front stagnation point corresponding to the formation of a thermal boundary layer, and in fact the maximum of the temperature gradient moves towards the front stagnation point as Pr increases and is located exactly at that point in the limit of infinite Péclet number (note the non-monotonic variation of the maximum gradient with h).

(The thickness of the boundary layer is expected to be of order $Pe^{-1/2}$ appropriate for a mobile interface, see e.g. Shraiman (1987) and Trevelyan *et al.* (2002). The

https://doi.org/10.1017/S0022112007008476 Published online by Cambridge University Press

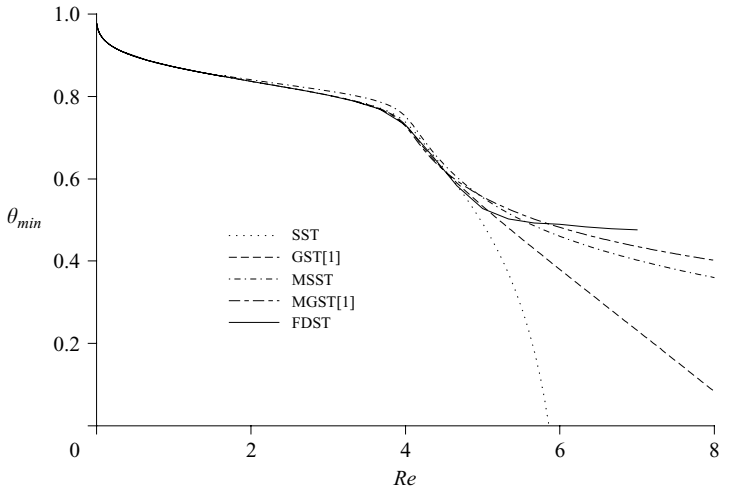


FIGURE 11. Comparison of the minimum interfacial temperature θ_{min} against Re obtained from the different models (see table 1) with FDST; $\hat{M}a = 0$, $\hat{B}i = 0.1$ and $Pr = 7$.

presence of a stagnation point where the boundary layer turns from the interface into the fluid and along the separatrix line as well as the presence of a free surface would make a singular perturbation analysis rather involved if not impossible (unlike e.g. Trevelyan *et al.* 2002).)

(The boundary layer appears at the front stagnation point because for large Pe (convection dominates over diffusion of heat) the flow in the moving frame transfers large amounts of heat on the free surface from either side of the stagnation point: to the left of the front stagnation point, we have a clockwise recirculation zone and hence $U > 0$ there, whereas to the right, $U < 0$. This can be easily seen by checking the sign of U on the flat-film region ahead of the front stagnation point: in this region $\psi = (3h - y)(y^2/6)$ so that $u|_{y=1} = 1/2$ and $U|_{y=1} = (1/2) - c < 0$ since $c \geqslant 1$).

We expect that in the presence of the Marangoni effect and for large Péclet numbers, the sharp spike in θ_Z will have a significant influence on the fluid flow. It is likely that, in this case, thermocapillarity might cause the formation of a recirculation zone at smaller Re and might tighten both streamlines and isotherms owing to enhancing the circulation in the primary solitary hump thus leading to both large temperature and velocity gradients in the flow.

8.2.1. *Comparison of different ST models with FDST*

Figure 11 compares the minimum of the interfacial temperature distribution θ_{min} for ST as a function of Re obtained from SST and GST[1] to that obtained from FDST. Once the recirculation zone appears at $Re = 4.5$, FDST falls rapidly to a value of $\theta_{min} = 0.47$ where it saturates as Re increases. The curve terminates at $Re = 7$ simply because of numerical difficulties with FDST at large Re.

Prior to the appearance of the recirculation zone, both SST and GST[1] accurately model FDST. However, soon after the birth of the recirculation zone, the SST model appears to diverge away from FDST almost quadratically as Re increases. On the other hand, the GST[1] model appears to follow FDST for a larger region of Reynolds numbers, but at some point it starts to diverge almost linearly, thus predicting higher interfacial temperatures than SST and closer to the actual values predicted by FDST.

https://doi.org/10.1017/S0022112007008476 Published online by Cambridge University Press

The new model GST[1] shows a marked improvement over the previous SST model. Nevertheless, despite the improvement, at some point the new model also starts to deviate from the actual interfacial temperature. In fact, both models give negative temperatures at some Re which are obviously unphysical: turning back to dimensional quantities, this would imply that the interfacial temperature can be locally smaller than the air temperature.

Clearly, the increased deviation between the interfacial temperature predicted by our models and the numerical solution of the two-dimensional energy equation is due to the formation of a boundary layer at the front stagnation point with large gradients in θ_Z as discussed in § 8.2. As a consequence, for large Re, all models overshoot the minimum temperature to give negative temperatures. In fact, any weighted residuals approach is bound to deviate from the actual temperature for large Re: to represent the temperature field accurately as the boundary layer develops, we would need an increasingly large number of test functions and thus amplitude equations.

8.3. *The modified SST and GST[1] models*

We note that as θ_{min} tends to zero for both SST and GST[1], the absolute value of the coefficient of θ_Z also becomes smaller and eventually passes through zero for both models. ($\theta_{min} < 0$ and the absolute value of the coefficient of θ_Z going through zero, do not necessarily occur at the same time, in general $\theta_{min} < 0$ occurs first). To test whether there is a link between the two, we develop models which prevent the absolute value of the coefficient of θ_Z in SST and GST[1] models from going through zero. This is accomplished by modifying appropriately the weight function for the energy equation. The modified SST and GST[1] models, referred to as MSST and MGST[1] models, respectively, are derived in Appendix D.

Figure 11 shows that the new travelling-wave models never predict negative temperatures. It then appears that there is a link between $\theta_{min} < 0$ and the absolute value of the coefficient of θ_Z passing through zero. Obviously, when the coefficient of θ_Z is exactly zero, the associated dynamical system has a singularity which would then cause some formidable difficulties in the numerical construction of the travelling waves. However, before this happens we do not encounter any difficulties in the numerical construction of the travelling waves and yet we have an increased divergence from FDST. Hence, the presence of negative temperatures is not due to numerical problems, but to the reduction of the coefficient of θ_Z.

It is important to emphasize that $\theta_{min} < 0$ appears earlier in the presence of the Marangoni effect, for example, in the bifurcation diagrams of figure 3(c); this will happen at some value of Re above the one corresponding to the appearance of a recirculation zone. The value of Re at which a recirculation zone forms decreases with increasing $\hat{M}a$. After the value of Re at which $\theta_{min} < 0$, the bifurcation diagrams for the speed of the solitary waves as a function of Re can be continued to larger Re while the temperature still remains negative (in fact, for $\hat{M}a = 0$, the continuation of the GST[1] curve in figure 3(c) will eventually lead to negative temperatures at some $Re > 8$ whereas the SST model has already developed negative temperatures at $Re \sim 6$). This continuation is possible at least up to the point where the coefficient of θ_Z vanishes (see our earlier discussion).

The values of Re where this happens, and for that matter the values of Re where a recirculation zone appears, are not far (at least for small $\hat{M}a$) from the region where the bifurcation curves for different $\hat{M}a$ predict speeds close to the final asymptotic value for large Re which coincides with the value obtained from the isothermal case (as we emphasized in § 6.2, as Re increases, $\hat{M}$ tends to zero and eventually the

https://doi.org/10.1017/S0022112007008476 Published online by Cambridge University Press

hydrodynamics is decoupled from the energy transport). Hence, the speed c of the solitary waves is predicted accurately at least when the bifurcation curves start approaching the isothermal asymptote and also prior to the development of a recirculation zone. It is precisely for this reason that we kept the momentum equation in (5.4) the same throughout this study: unphysical temperatures originate from the treatment of the energy equation and not the momentum equation.

Figure 11 indicates that both MSST and MGST[1] offer a substantial improvement over the SST and GST[1] models. This is because these models have eliminated the deficiency from which the SST and GST[1] models suffer, i.e. the reduction of the absolute value of the coefficient of θ_Z. Nevertheless, a divergence (albeit slow) from FDST is also observed for MSST and MGST[1] and eventually these models level off at some θ_{min} value lower than that predicted by FDST. Again, this is due to the development of a thermal boundary layer at the front stagnation point.

9. Conclusion

We have analysed the dynamics of a film falling down a heated wall. We considered two types of wall boundary conditions: heat flux (HF) and specified temperature (ST). The flow and heat transport were first modelled with a long-wave theory for large Péclet numbers. We subsequently developed averaged models using a weighted residuals approach. In these models, the flow was modelled via a first order in ϵ single-mode Galerkin approximation of the momentum equation. The transport of heat was modelled in two ways: (i) a simple first order in ϵ weighted residuals approximation with a single test function which does not satisfy all boundary conditions; (ii) a refined treatment of the energy equation by using a first order in ϵ Galerkin approximation based on a set of test functions that satisfy all boundary conditions.

We examined the solitary-wave solutions of the long-wave theory and the models obtained from the simple weighted residuals and single-mode Galerkin projections for both HF and ST cases. The bifurcation diagrams for the speed of the solitary waves as a function of Reynolds number obtained from the long-wave theory are unrealistic with turning points and branch multiplicity (a lower branch and upper branch) or points where the solution branches terminate. On the other hand, our averaged models show the continuing existence of solitary waves for all Reynolds numbers. The HF averaged models in particular show the existence of both positive- and negative-hump solitary waves, unlike the ST ones which yield only positive-hump waves. The averaged models are also robust in time-dependent computations. These computations reveal that sufficiently large Péclet numbers bring about an organization of the free surface which otherwise exhibits a complex spatio-temporal dynamics reminiscent of the KS chaos.

Subsequently, we compared the interfacial temperature distribution obtained from our averaged models to that obtained from the full (first order in ϵ) energy equation. The single-mode Galerkin projections are in good agreement with the actual solution and provide a substantial improvement for the interfacial temperature over the simple weighted residuals models as the Reynolds number increases. The agreement persists up to a certain Reynolds number, at which point a recirculation zone appears in the primary solitary hump. Further increase of the Reynolds number leads to the development of a thermal boundary layer at the front stagnation point which results in an increased deviation from the actual interfacial temperature, but at a rate slower than that observed for the simple weighted residuals models which diverge first.

https://doi.org/10.1017/S0022112007008476 Published online by Cambridge University Press

Eventually, all models predict negative interfacial temperatures at some Reynolds number. This deficiency was attributed to the coefficient of interfacial temperature derivative with respect to the moving coordinate going through zero and was cured with the introduction of modified weight functions prior to averaging. The resulting modified averaged models prevent the interfacial temperature from going negative and showed a marked improvement over the previous averaged models. Nevertheless, the modified models also deviate from the full energy equation, again owing to the presence of the boundary layer.

The recirculation zone below a primary solitary hump is physical and does not invalidate the long-wave assumption which forms the basis of any boundary-layer approximation. It is the thermal boundary layer at the front stagnation point connected with large gradients of the interfacial temperature which is not allowed within the long-wave framework. Therefore, thermal boundary layers are signs of the breakdown of the theory presented here. However, it is likely that the two-dimensional flow cannot sustain a sharp boundary layer and will attempt to diffuse it in the transverse direction with a development of a three-dimensional instability. The system then naturally relaxes the strong gradients of interfacial temperature.

We are grateful to Professors Paul Manneville and Manuel Velarde for stimulating discussions. We acknowledge financial support from the Engineering and Physical Sciences Research Council of England through grant GR/S01023 and an Advanced Research Fellowship, grant GR/S49520.

Appendix A. Large-Péclet-number LWE solutions

The temperature field is given by

$$\begin{aligned}\text{HF: } T &= [1+B(h-y)]F - PeB_wBF^2h_xy^4\left(\frac{3By}{40}-\frac{1}{8}-\frac{3B}{8}h\right)\\ &\quad - PeB^2F^2hh_xy^2\left[(B_wh-1)\frac{y}{2}+\frac{3h}{2}\right]\\ &\quad + PeB(1+B_wy)F^3h^3h_x\left[\frac{B^2}{5}h(5+B_wh)+\frac{B_w}{4}(Bh-2)+\frac{3}{2}B\right], \quad (A\,1a)\\ \text{ST: } T &= (1+\hat{B}(h-y))\hat{F} - Pe\hat{B}\hat{F}^2h_xy^3\left[\frac{3\hat{B}}{40}y^2-\left(\frac{1}{8}+\frac{3\hat{B}}{8}h\right)y+\frac{\hat{B}}{2}h^2\right]\\ &\quad + Pe\hat{B}\hat{F}^3h^3h_xy\left(\frac{\hat{B}^2}{5}h^2+\frac{\hat{B}}{4}h-\frac{1}{2}\right), \quad (A\,1b)\end{aligned}$$

where

$$F=(B+B_w+BB_wh)^{-1}, \quad \hat{F}=(1+\hat{B}h)^{-1}.$$

Notice that setting $h=1$ in F and $\hat{F}$ yields the definitions of $\overline{F}$ and $\overline{\hat{F}}$ in § 3. By taking the leading-order terms from the limit of infinite B_w, $T_{\mathrm{HF}}=(1/B_w)T_{\mathrm{ST}}$. Returning to dimensional variables, $(T-T_a)/(q_0l_0/\lambda)=(1/Bi_w)(T-T_a)/(T_w-T_a)$ or $q_0=\alpha_w(T_w-T_a)$ as expected since in the limit $B_w\to\infty$ the ST and HF problems are identical (see § 2.3).

The streamfunction is given by

$$\begin{aligned}\text{HF: } \psi &= (1+We h_{xxx}-h_x\cot\beta)(3h-y)\frac{y^2}{6}+\frac{Re}{40}(20h^3-5hy^2+y^3)hh_xy^2\\ &\quad + \frac{M}{2}B_wBF^2h_xy^2-\frac{Pe}{80}MB(Gh^3h_x)_xy^2. \quad (A\,2)\end{aligned}$$

https://doi.org/10.1017/S0022112007008476 Published online by Cambridge University Press

For ST, the streamfunction is given by (A 2) with $(G, MB_wBF^2, MB) \to (\hat{G}, \hat{M}\hat{B}\hat{F}^2, \hat{M}\hat{B})$. The functionals G and $\hat{G}$ are due to the convective heat transport effects and are given by

$$G = 7(4 + B_w h)F^2 + \left(32B - 22B_w^2 h - 48B_w\right)F^3 \quad \text{and} \quad \hat{G} = (7\hat{B}h - 15)h\hat{F}^3.$$

In the limit of infinite B_w, $B_w F \to \hat{F}$ and $B_w G \to \hat{G}$. It is also useful to examine the limit of very thin films, i.e. $\bar{h}_N \to 0$. The convective functionals yield

$$G\bar{h}_N^2 \to 20\frac{(3Bi - Bi_w)}{(Bi + Bi_w)^3} + O(\bar{h}_N) \quad \text{and} \quad \hat{G} \to -15h + O(\bar{h}_N),$$

which shows that in this limit $\hat{G} < 0$ whereas $G \gtrless 0$ for $Bi_w/Bi \lesseqgtr 3$.

Appendix B. The GHF[1] and GST[1] models

The GHF[1] model consists of (5.1*c*), (5.4) and the following equation for θ:

$$\begin{aligned}
&\left[120 + 10\left(B_w^2 - 5B_wB + B^2\right)h^2 + 5(16 - B_wBh^2)\frac{h}{F} + \frac{6h^2}{F^2}\right]\frac{\theta_t}{30} \\
&\quad + \left[80 + 55B_wh + 35Bh + (3B_w + 2B)^2h^2 + (9 + 4B_wh + 3Bh)\frac{h}{F} + \frac{5h^2}{7F^2}\right]\frac{q\theta_x}{20h} \\
&\quad - \left(92B - 64B_w + 30B^2h + 25B_wBh - 17B_w^2h + \frac{4B_w + 15B}{F}h + \frac{27h}{7F^2}\right)\frac{\theta q_x}{120} \\
&\quad - \left[\frac{B^2h + 4B - 2B_w}{2 + B_wh}\theta + \frac{2 + Bh}{2 + B_wh} + \frac{4}{21}(7 + B_wh) + \frac{11B}{168}(8 + B_wh)\right]\frac{2q_x}{5} \\
&\quad + \left[324B - 96B_w - 84B_w^2h - (56B_w + 43B)B_wBh^2 - \frac{16 + 74B_wBh^2}{F}\right]\frac{\theta q h_x}{280h} \\
&\quad + \left[\frac{21}{F^2} + 12\frac{(B_w - B)^2}{2 + B_wh}\right]\frac{\theta q h_x}{70h} + \left(32 + 11Bh + 24\frac{2 + Bh}{2 + B_wh}\right)\frac{qh_x}{140} \\
&\quad + [12 + 4(B_w + B)h + B_wBh^2]\frac{\theta F^{-1} - 1}{9Peh} = 0.
\end{aligned} \tag{B 1a}$$

The GST[1] model consists of (5.1*c*), (5.4) and the following equation for θ:

$$\begin{aligned}
&(51 + 18\hat{B}h + 2\hat{B}^2h^2)\frac{h\theta_t}{105} + (2137 + 698\hat{B}h + 73\hat{B}^2h^2)\frac{q\theta_x}{3360} \\
&\quad + \left[\left(\frac{101}{1344} - \frac{227}{3360}h\hat{B} - \frac{17}{960}\hat{B}^2h^2\right)\theta - \frac{101}{1344} - \frac{19}{960}\hat{B}h\right]q_x + (349 + 73\hat{B}h)\frac{\hat{B}\theta q h_x}{3360} \\
&\quad + (6 + \hat{B}h)\frac{\theta\hat{F}^{-1} - 1}{15Peh} = 0.
\end{aligned} \tag{B 1b}$$

Appendix C. Analysis of linearized travelling-wave equations

Analysing the linearized wave equations allows the derivation of necessary conditions for the existence of solitary waves and sufficient conditions for their non-existence.

C.1. *LWE*

The limit point where the long-wave solution branch terminates in figure 3(*a*) can be explained by examining a linearized form of the corresponding long-wave

https://doi.org/10.1017/S0022112007008476 Published online by Cambridge University Press

equation. Substituting $h = 1 + \hat{h}\exp(\Lambda Z)$ into the LWE-HF travelling-wave model and linearizing for $\hat{h} \ll 1$ yields

$$\Lambda^3 + 3\overline{\mathscr{C}}\Lambda^2 + 3\overline{\mathscr{A}}\Lambda + 3(1-c) = 0. \tag{C 1}$$

When all the roots Λ have real parts of the same sign, it is impossible for solitary-wave solutions of the LWE-SHF travelling-wave model to exist. Consider now a cubic equation of the general form $z^3 + a_2z^2 + a_1z + a_0 = 0$. When $a_0 = a_2a_1$, the cubic can be expressed as $(z + a_2)(z^2 + a_1) = 0$. Thus, if $a_1 > 0$, the cubic has two purely imaginary roots. Returning to (C 1), a pair of purely imaginary roots exists at $c = c^*$ (Hopf bifurcation) where

$$c^* = 1 - 3\overline{\mathscr{A}\mathscr{C}}, \tag{C 2}$$

with $\overline{\mathscr{A}} > 0$ (we require $\overline{\mathscr{A}} > 0$ for $Re > Re_c$). We note that (C 1) has a zero root when $c = 1$ which is the kinematic wave velocity. A sufficient and necessary condition now for positive solitary waves not to exist is $c \leqslant c^*$. At the point where the solitary-wave solution branch in figure 3(*a*) terminates we have $c = c^*$.

When $\overline{\mathscr{C}} > 0$, a pair of purely imaginary roots exists only when $c = c^* < 1$, i.e. for negative solitary waves. Similarly, when $\overline{\mathscr{C}} < 0$, a pair of purely imaginary roots only exists when $c = c^* > 1$, i.e. for positive solitary waves. Two necessary conditions for positive solitary waves to exist are $c > 1$ and $c > c^*$.

C.2. *SHF and SST*

Substitution of $h = 1 + \hat{h}\exp(\Lambda Z)$ and $\theta = \overline{F} + \hat{\theta}\exp(\Lambda Z)$ into the SHF travelling-wave model and linearizing for $\hat{h}, \hat{\theta} \ll 1$ yields

$$\left[\Lambda^3 + \Lambda\left(\frac{2\delta}{35}(21c^2 - 17c + 3) - \zeta\right) + 3(1-c)\right]\hat{h} - \tfrac{3}{2}\mathscr{M}\Lambda\hat{\theta} = 0. \tag{C 3}$$

$$\left(B_w - \frac{c(5+B_w)-1}{8}Pr\delta\Lambda\right)B\hat{h} + \left[\frac{1}{\overline{F}} + \left(\tfrac{1}{3} - c + \tfrac{5}{24}B_w - \tfrac{1}{2}B_wc\right)Pr\delta\Lambda\right]\frac{\hat{\theta}}{\overline{F}} = 0. \tag{C 4}$$

For SST, (C 4) is replaced by

$$\left(1 - \frac{7cPr\delta\Lambda}{120}\right)\hat{B}\hat{h} + \left[\frac{1}{\hat{F}} + \left(\tfrac{3}{20} - \tfrac{c}{3}\right)Pr\delta\Lambda\right]\frac{\hat{\theta}}{\hat{F}} = 0. \tag{C 5}$$

By eliminating $\hat{h}$ and $\hat{\theta}$, we obtain a quartic dispersion relation for both SHF and SST, of the form $z^4 + a_3z^3 + a_2z^2 + a_1z + a_0 = 0$. Sufficient and necessary conditions for all roots of this polynomial to have negative real parts can be obtained with an extension of the Routh–Hurwitz theorem (Strelitz 1977). For a quartic, the result is $a_3 > 0$, $a_2 > 0$, $0 < a_1 < a_2a_3$ and $0 < a_0 < (a_1a_2a_3 - a_1^2)/a_3^2$. With $z \to -z$, we can then obtain the sufficient and necessary conditions for all roots to have positive real parts. By simply changing the sign of a_1 and a_3 in the previous conditions, the new conditions are $a_3 < 0$, $a_2 > 0$, $a_2a_3 < a_1 < 0$ and $0 < a_0 < (a_1a_2a_3 - a_1^2)/a_3^2$. These two sets of inequalities define two regions, say R_1 and R_2 in the fourth-dimensional space $\{a_0, a_1, a_2, a_3\}$. In $R_1 \bigcup R_2$ all roots have real parts of the same sign and hence it is impossible for solitary waves to exist there. Hence, a necessary condition for solitary waves to exist is that the roots lie outside $R_1 \bigcup R_2$.

https://doi.org/10.1017/S0022112007008476 Published online by Cambridge University Press

Appendix D. Modified travelling-wave models

The coefficient of the interfacial temperature derivative with respect to the travelling-wave coordinate $z = x - ct$ in the single-mode Galerkin projection is given by $\int_0^1 (u^{(0)} - c)\phi_1^2 \, \mathrm{d}\eta$. As the interfacial waves become larger, the flow becomes faster so that the term $u^{(0)} - c$ which is strictly negative for small-amplitude waves, passes through zero and becomes positive. Note that in the absence of Marangoni effects, $u^{(0)} = c$ on the interface when $h = 3 - (2/c)$, which marks the location of the stagnation points for the largest solitary waves; see also § 8.1. Hence, as the height of the waves increases, $\int_0^1 (u^{(0)} - c)\phi_1^2 \, \mathrm{d}\eta$ can change sign and become positive. Note that as we pointed out in § 8.1, the condition $u^{(0)} = c$ does not violate the long-wave approximation.

To alleviate the difficulties associated with a zero coefficient, we appropriately modify our projection approach. More specifically, we introduce the weight function

$$w_1 = \left(u^{(0)} - c\right)\phi_1$$

so that the coefficient of θ_Z becomes $\int_0^1 (u^{(0)} - c)^2 \phi_1^2 \, \mathrm{d}\eta$ which is non-negative. Hence, by multiplying the weight function in GST[1] by $(u - c)$ we obtain the 'modified GST[1]' model which we denote by MGST[1]:

$$\begin{aligned} 0 \;=\; & \left(\frac{5287}{144} + \frac{45}{4}\hat{B}h + \frac{161}{144}\hat{B}^2h^2\right)(3c-1)^2\theta' - \left(\frac{8215}{144} + \frac{1021}{72}\hat{B}h + \frac{163}{144}\hat{B}^2h^2\right) \\ & \times (3c-1)ch\theta' + \left(\frac{665}{24} + \frac{175}{24}\hat{B}h + \frac{2}{3}\hat{B}^2h^2\right)c^2h^2\theta' \\ & + \left(\frac{301}{192}ch - \frac{61}{6}(3c-1)\right)(\theta-1)ch' + \frac{101\theta - 2}{96}c^2h^2\hat{B}h' \\ & + \left[\left(\frac{45}{8} + \frac{161}{144}\hat{B}h\right)(3c-1)^2 + \left(\frac{11}{64}ch - \frac{41}{36}(3c-1)\right)\hat{B}ch^2\right]\hat{B}\theta h' \\ & + \frac{11}{8Pr\delta h}(\theta\hat{F}^{-1} - 1)[(149 + 23\hat{B}h)(1-3c) + (111 + 13\hat{B}h)ch]. \end{aligned} \tag{D 1}$$

Similarly, by multiplying the weight function in SST by $(u - c)$ and using integration by parts in a similar way to the derivation of SST, we obtain the 'modified SST' model which we denote by MSST:

$$\begin{aligned} 0 \;=\; & \left(\frac{29}{20}(3c-1)^2 + \frac{12}{5}(1-3c)ch + \frac{27}{20}c^2h^2\right)\theta' + \left(19(1-3c) + \frac{2231}{40}ch\right)(\theta-1)ch' \\ & + \frac{7}{6Pr\delta h}(\theta\hat{F}^{-1} - 1)(1 - 3c + ch). \end{aligned} \tag{D 2}$$

The time-dependent analogues of these models can be obtained by multiplying the energy equation by $\theta_t + u^{(0)}\theta_x$ prior to averaging. The resulting averaged equations involve θ_t^2, θ_x^2 and $\theta_t\theta_x$. For example, the ST model is of the form

$$\begin{aligned} & a_1\theta_t^2 + a_2\frac{q}{h}\theta_t\theta_x + a_3\frac{q^2}{h^2}\theta_x^2 + \frac{q}{h^2}\theta_x\left(q_x\left[a_4 + a_5\theta\right] + a_6qh_x\theta\right) \\ & \quad + \frac{\theta_t}{h}\left(q_x\left[a_7 + a_8\theta\right] + a_9qh_x\theta\right) + \frac{\theta\hat{F}^{-1} - 1}{Peh^2}\left(a_{10}\theta_t + a_{11}\frac{q}{h}\theta_x\right) = 0, \end{aligned}$$

with $a_i = a_i(h; \hat{B})$.

https://doi.org/10.1017/S0022112007008476 Published online by Cambridge University Press

REFERENCES

Benjamin, T. B. 1957 Wave formation in laminar flow down an inclined plane. *J. Fluid Mech.* **2**, 554–574.

Benney, D. J. 1966 Long waves on liquid films. *J. Math. Phys.* **45**, 150–155.

Chang, H.-C. & Demekhin, E. A. 2002 *Complex Wave Dynamics on Thin Films*. Elsevier.

Demekhin, E. A., Kaplan, M. A. & Shkadov, V. Ya. 1987 Mathematical models of the theory of viscous liquid films. *Izv. Akad. Nauk SSSR, Mekh. Zhidk i Gaza* **6**, 9–16.

Doedel, E., Champneys, A., Fairfrieve, T., Kuznetsov, Y., Sandstede, B. & Wang, X. 1997 *Auto 97 Continuation and Bifurcation Software for Ordinary Differential Equations*. Montreal Concordia University.

Goodwin, R. & Homsy, G. M. 1991 Viscous flow down a slope in the vicinity of a contact line. *Phys. Fluids* **3**, 515–528.

Gottlieb, D. & Orszag, S. A. 1977 *Numerical Analysis of Spectral Methods: Theory and Applications*. SIAM.

Goussis, D. A. & Kelly, R. E. 1991 Surface waves and thermocapillary instabilities in a liquid film flow. *J. Fluid Mech.* **223**, 24–45.

Joo, S. W., Davis, S. H. & Bankoff, S. G. 1991 Long-wave instabilities of heated falling films: two-dimensional theory of uniform layers. *J. Fluid Mech.* **230**, 117–146.

Kabov, O. A. 1998 Formation of regular structures in a falling liquid film upon local heating. *Thermophys. Aeromech.* **5**, 547–551.

Kabov, O. A., Legros, J. K., Marchuk, I. V. & Scheid, B. 2000 Deformation of the free surface in a moving locally-heated thin liquid layer. *Izv. Akad. Nauk SSSR, Mekh. Zhidk Gaza* **3**, 200–208.

Kalliadasis, S., Kiyashko, A. & Demekhin, E. A. 2003*a* Marangoni instability of a thin liquid film heated from below by a local heat source. *J. Fluid Mech.* **475**, 377–408.

Kalliadasis, S., Demekhin, E. A., Ruyer-Quil, C. & Velarde, M. G. 2003*b* Thermocapillary instability and wave formation on a film falling down a uniformly heated plane. *J. Fluid Mech.* **492**, 303–338.

Kapitza, P. L. 1948 Wave flow of thin layers of a viscous fluid. *Sov. Phys. J. Exp. Theor. Phys.* **18**, 3–28.

Kapitza, P. L. & Kapitza, S. P. 1949 Wave flow of thin layers of a viscous fluid: III. Experimental study of undulatory flow conditions. *Sov. Phys. J. Exp. Theor. Phys.* **19**, 105–120.

Kawahara, T. 1983 Formation of saturated solitons in a nonlinear dispersive system with instability and dissipation. *Phys. Rev. Lett.* **51**, 381–383.

Nakaya, C. 1989 Waves on a viscous fluid film down a vertical wall. *Phys. Fluids* A **1** (7), 1143–1154.

Oron, A., Davis, S. H. & Bankoff, S. G. 1997 Long-scale evolution of thin liquid films. *Rev. Mod. Phys.* **69**, 931–980.

Pumir, A., Manneville, P. & Pomeau, Y. 1983 On solitary waves running down an inclined plane. *J. Fluid Mech.* **135**, 27–50.

Ramaswamy, B., Chippada, S. & Joo, S. W. 1996 A full-scale numerical study of interfacial instabilities in thin film flows. *J. Fluid Mech.* **325**, 163–194.

Ruyer-Quil, C. & Manneville, P. 2000 Improved modeling of flows down inclined planes. *Eur. Phys. J.* B **15**, 357–369.

Ruyer-Quil, C. & Manneville, P. 2002 Further accuracy and convergence results of the modeling of flows down inclined planes by weighted residual approximations. *Phys. Fluids* **14**, 170–183.

Ruyer-Quil, C., Scheid, B., Kalliadasis, S., Velarde, M. G. & Zeytounian, R. Kh. 2005 Thermocapillary long waves in a liquid film flow. Part 1. Low-dimensional formulation. *J. Fluid Mech.* **538**, 199–222.

Salamon, T. R., Armstrong, R. C. & Brown, R. A. 1994 Travelling waves on vertical films: numerical analysis using the finite element method. *Phys. Fluids* **6** (6), 2202–2220.

Scheid, B. 2004 Evolution and stability of falling liquid films with thermocapillary effects. PhD thesis, Université Libre de Bruxelles.

Scheid, B., Oron, A., Colinet, P., Thiele, U. & Legros, J. C. 2002 Nonlinear evolution of nonuniformly heated falling liquid films. *Phys. Fluids* **14** (12), 4130–4151.

https://doi.org/10.1017/S0022112007008476 Published online by Cambridge University Press

Scheid, B., Ruyer-Quil, C., Thiele U., Kabov, O. A., Legros, J. C. & Colinet, P. 2004 Validity domain of the Benney equation including Marangoni effect for closed and open flows. *J. Fluid Mech.* **527**, 303–335.

Scheid, B., Ruyer-Quil, C., Kalliadasis, S., Velarde, M. G. & Zeytounian, R. Kh. 2005 Thermocapillary long waves in a liquid film flow. Part 2. Linear stability and nonlinear waves. *J. Fluid Mech.* **538**, 223–244.

Shkadov, V. Ya. 1967 Wave models in the flow of a thin layer of a viscous liquid under the action of gravity. *Izv. Akad. Nauk SSSR, Mekh. Zhidki Gaza* **1**, 43–50.

Shkadov, V. Ya. 1968 Theory of wave flow of a thin layer of a viscous liquid. *Izv. Akad. Nauk SSSR, Mekh. Zhidki Gaza* **2**, 20–25.

Shkadov, V. Ya. 1977 Solitary waves in a layer of viscous liquid. *Izv. Akad. Nauk SSSR, Mekh. Zhidki Gaza* **12**, 63–66.

Shraiman, B. 1987 Diffusive transport in a Rayleigh–Bénard convection cell. *Phys. Rev.* A **36**, 261–267.

Smith, K. A. 1966 On convective instability induced by surface-tension gradients. *J. Fluid Mech.* **14**, 401–414.

Strelitz, S. 1977 On the Routh–Hurwitz problem. *Am. Math. Mon.* **84**, 542–544.

Trevelyan, P. M. J. & Kalliadasis, S. 2004 Dynamics of a reactive falling film at large Péclet numbers. I. Long-wave approximation. *Phys. Fluids* **16** (8), 3191–3208.

Trevelyan, P. M. J., Kalliadasis, S., Merkin, J. H. & Scott, S. K. 2002 Mass transport enhancement in regions bounded by rigid walls. *J. Engng Maths* **42**, 45–64.

Yih, C.-S. 1963 Stability of liquid flow down an inclined plane. *Phys. Fluids* **6** (3), 321–334.

https://doi.org/10.1017/S0022112007008476 Published online by Cambridge University Press